Nuclear Instruments and Methods in Physics Research A 336 (1993) 23–52
North-Holland

NUCLEAR
INSTRUMENTS
& METHODS
IN PHYSICS
RESEARCH
Section A

Beam tests of the ZEUS barrel calorimeter

A. Bernstein [b], T. Bienz [c], A. Caldwell [b], L. Chen [d], M. Derrick [a], I. Gialas [b], A. Hamri [c], R. Imlay [d], S. Kartik [d], H.J. Kim [d], T. Kinnel [h], H. Kreutzmann [c], C.G. Li [e], J.N. Lim [f], R. Loveless [h], B. Lu [g], U. Mallik [c], K.W. McLean [e], R. McNeil [d], W. Metcalf [d], B. Musgrave [a], B.Y. Oh [f], S. Park [e], J.A. Parsons [b], D. Reeder [h], J. Repond [a], S. Ritz [b], M.T.P. Roco [c], P.H. Sandler [h], F. Sciulli [b], W.H. Smith [h], R.L. Talaga [a], G. Tzanakos [b,1], L. Wai [b], M.Z. Wang [c], J. Whitmore [f], J. Wu [c] and S. Yang [b]

[a] *Argonne National Laboratory, Argonne, IL, USA*
[b] *Columbia University, New York, NY, USA, and Nevis Laboratories, Irvington-on-Hudson, NY, USA*
[c] *University of Iowa, Iowa City, IA, USA*
[d] *Louisiana State University, Baton Rouge, LA, USA*
[e] *Ohio State University, Columbus, OH, USA*
[f] *Pennsylvania State University, University Park, PA, USA*
[g] *Virginia Polytechnic Institute, and State University, Blacksburg, VA, USA*
[h] *University of Wisconsin, Madison, WI, USA*

Received 30 June 1993

A fully compensating uranium–scintillator calorimeter was constructed for the ZEUS detector at HERA. Several of the barrel calorimeter modules were subjected to beam tests at Fermilab before shipping them to DESY for installation The calibrations of the modules used beams of electrons and hadrons, measuring the uniformity of the response, and checking the resolution. The runs also provided opportunity to test a large fraction of the actual ZEUS calorimeter readout system in an integrated beam environment more than one year before HERA turn on. The experiment utilized two computer controlled mechanical structures, one of which was capable of holding up to four modules in order to study shower containment, and a magnetic spectrometer with a high resolution beam tracking system. During two running periods, beams of 6 to 110 GeV containing e, μ, π, and $\bar{p}$ were used. The results show energy resolutions of $35\%/\sqrt{E}$ for hadrons and $19\%/\sqrt{E}$ for electrons, uniformities at the 1% level, energy nonlinearity less than 1%, and equal response for electrons and hadrons.

1. Introduction

Several modules of the ZEUS barrel calorimeter (BCAL) were tested and calibrated in a Fermilab test beam during 1990 and 1991. We report here on this experiment, E790, and the results of the data analysis.

The ZEUS calorimeter was designed to have an optimal hadronic resolution, and operate in the unique environment of the asymmetric HERA e–p collider. The asymmetry requirement is most clearly manifested in the main component of the detector, the depleted uranium (DU)-scintillator electromagnetic and hadronic calorimeter with a depth ranging from about 7 interaction lengths λ_I in the forward calorimeter (FCAL) to about 5 λ_I in the BCAL to 4 λ_I in the rear calorimeter (RCAL). Forward and rear refer to the proton and electron directions respectively. To optimize the hadronic energy resolution the geometry of the unit cell of the calorimeter was carefully selected so that compensation was achieved [1]. The calorimeter is nearly hermetic, covering 2π in azimuth and polar angles between 2.2° and 176.5°. The readout electronics were specially designed to handle the 96 ns HERA crossing rate and high backgrounds from p–gas interactions. One important aspect of the ZEUS calorimeter is the use of the natural radioactivity of the uranium as a stable calibration tool for signal normalization and for monitoring of the calorimeter gain.

For the test beam measurements, modules from the BCAL could be mounted on two computer controlled movable stands. One, while holding up to four mod-

[1] On leave from University of Athens, Greece.

ules, could rotate about a point analogous to the ZEUS interaction point. A backing calorimeter was used to measure leakage behind the BCAL modules. The second stand, positioned behind the backing calorimeter, could hold one module to study the response of the hadronic calorimeter (HAC) towers to muons. A magnetic spectrometer with scintillation counters and drift chambers was used to measure the beam particle momentum. The particle identity was established by transition radiation detectors (TRD), Cherenkov counters and the backing calorimeter. Data were taken with pions, electrons, muons, and antiprotons of various energies. The stability of the electronics and the calorimeter, the tower uniformity, position dependence, the light yield, and the system performance were studied in detail. The linearity of the calorimeter, the absolute calibration when exposed to electrons and hadrons and the electromagnetic and hadronic energy resolutions were measured.

The calorimeter systems have been extensively tested over a number of years. Early partial tests of individual subsystems [2] led to beam tests of F/RCAL completed modules at CERN [3], BCAL module testing with cosmic rays at Argonne [4], and later to the BCAL module beam tests at Fermilab reported here.

The next section describes the geometry, construction, and subsystems of the BCAL. The third section describes the various elements, both hardware and software, of the experiment. The fourth section describes the initial steps taken to insure the validity of the data. The fifth section includes all the results of the analysis, and the conclusion lists the most important results of this experiment.

2. BCAL

The BCAL consists of 32 identical modules. Each module covers the polar angle region from 36.7° to 129.1° and spans 11.25° in azimuth.

2.1. Module construction

Details of the design and construction of the BCAL modules may be found in ref. [5]. Each BCAL module is 330 cm in length, and extends from an inner radius of 123.2 cm to an outer radius of 291.2 cm in the ZEUS detector. The total depth of the BCAL corresponds to 5 interaction lengths for normal incidence. Each module is divided longitudinally into three sections which are read out independently, forming one electromagnetic (EMC) and two hadronic (HAC1, HAC2) calorimeter sections.

Each section of the BCAL is constructed from 3.3 mm thick DU plates with maximum difference of 0.25 mm, and (2.6 ± 0.07) mm thick SCSN-38 scintillator tiles. The DU plates are clad with stainless steel, and held apart by spacers located between adjacent scintillator tiles and spanning the whole width of the module.

The EMC section consists of 53 towers projective in polar angle, with front face dimensions of 49×233 mm^2. Each tower contains 21 DU plates and 22 layers

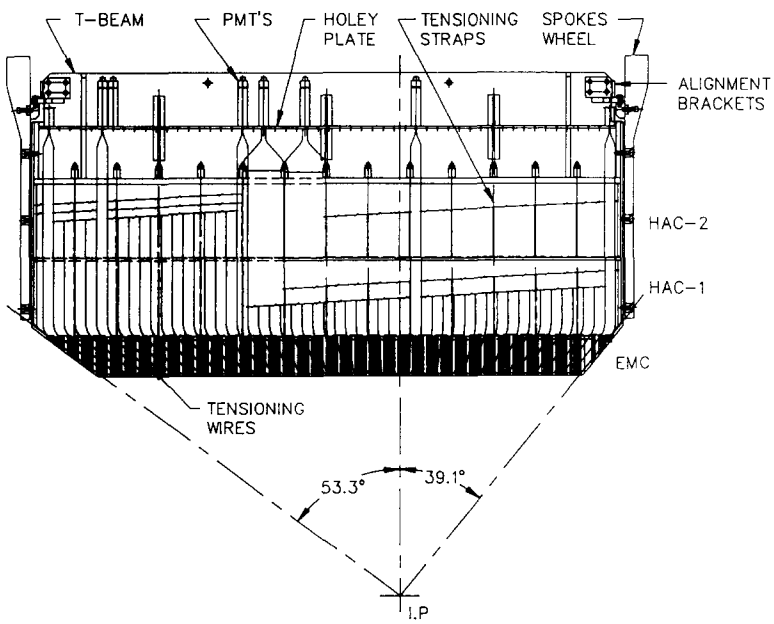

Fig 1. Side view of a BCAL module The three sections EMC, HAC1 and HAC2 are indicated.

of scintillator, corresponding to 21 radiation lengths (X_0) or about one interaction length (λ_1). The front plate is aluminum of thickness 10 mm. An empty thin-walled aluminum box is inserted between the fourth layer of scintillator and the fourth DU plate to house a future fine-grained detector located at the maximum of the electromagnetic showers.

The 14 HAC towers are non-projective and, with the exception of those at the ends, the scintillator plates of the first layer measure 244×271 mm^2. Each HAC section contains 49 DU plates and 50 layers of scintillator, corresponding to a depth of about $2\lambda_1$. The EMC and HAC1 sections are separated by a 10 mm thick aluminum plate, the EMC rear plate, and a 14.5 mm steel plate, the HAC1 front plate. A 17 mm ($1X_0$) steel plate separates the HAC1 and HAC2 sections.

Throughout most of the BCAL, four EMC towers encompass one HAC tower. However, the forward (rear) HAC tower is narrower in width and covers only 2(3) EMC towers. The EMC towers are numbered from 3 to 55, and the HAC towers from 1 to 14, as one proceeds from the FCAL end to the RCAL end.

The structural integrity of a module is provided by a frame consisting of a backbeam (T-beam) to which is bolted and pinned a front and rear end plate forming, together with the HAC1 front plate and the HAC1–HAC2 separator plate, a box for the HAC sections. The backbeam also conveniently houses the PMTs and their magnetic shielding, together with the front end readout and trigger electronics cards, and high voltage controller system. A side view of a module mounted between the supporting rings (spokesplates) of the BCAL is shown in fig. 1.

The DU plates were clad in stainless steel for several reasons; to minimize radiation damage to the SCSN-38 scintillator, and to reduce the scintillator light output to levels appropriate to acceptable photomultiplier tube (PMT) lifetime and noise, while retaining the average radioactivity signal as a useful calibration of gain and monitor of module performance. The cladding thickness was chosen to be 0.2 mm in the EMC and 0.4 mm in the HAC sections, constant to within 2.5 μm.

The scintillator tiles were individually wrapped in a 0.5 mm mirror finished aluminum foil [6]. In addition, to reduce the enhanced light output at the edges, each end was wrapped with a 30 mm wide strip of black Tedlar. The light output from the tile center to each end is then uniform to within 5%. The mean light output of each tile was measured by scanning with a collimated cobalt ^{60}Co radioactive source. This information was used in constructing masks placed behind the wavelength shifter plates to insure uniform response in depth.

Light produced in the scintillator is read out by the standard technique of wavelength shifting, using plastic panels that also guide the light to the back of the calorimeter [6]. Calorimeter towers are viewed by two

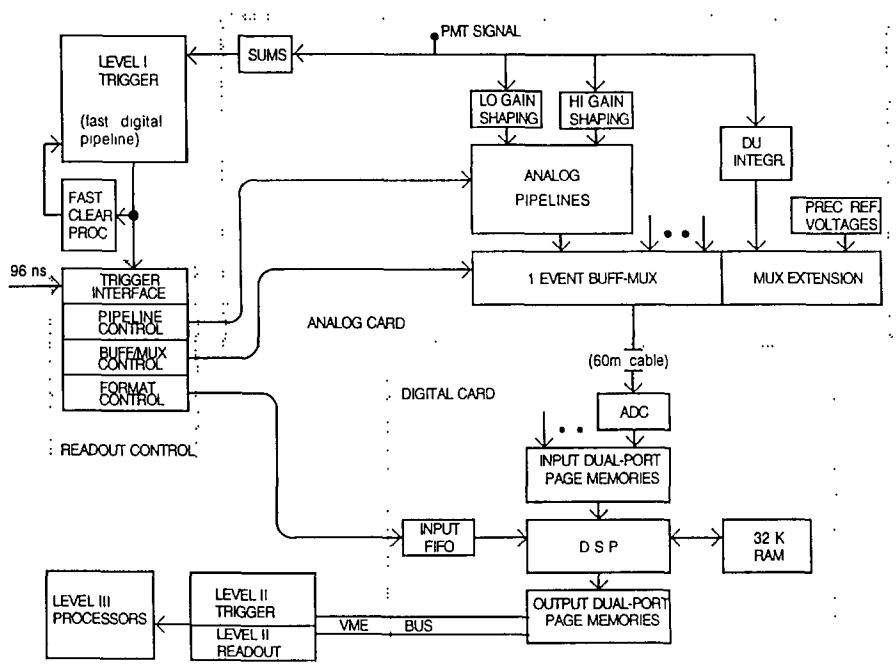

Fig. 2. Overview of ZEUS calorimeter read out scheme. The analog cards reside on the calorimeter modules while the digital cards and the NIM control modules are placed in the electronics hut.

wavelength shifter panels connected to separate Hamamatsu R580 photomultiplier tubes (PMTs), providing readout redundancy. The panels are Y7-doped (30 ppm) PMMA of nominal thickness 2.0 mm with an allowed variation of up to 0.4 mm. The surfaces of each wavelength shifter panel (WLS) not exposed to scintillator were wrapped in aluminum foil.

The design of the WLS system incorporated techniques to minimize non-uniformities in lateral light collection efficiency which, if uncorrected, would increase rapidly as the polar angle departs from 90°. Residual optical non-uniformities were removed using detailed light source scans of the active area of each light guide to construct a correction map. This map was transferred to a reflective medium. The active area of each WLS was then backed by this reflecting mask to remove non-uniformities due to light guide geometry, scintillator layer-to-layer light variations and DU plate thickness variations. The calorimeter modules are expected to have about 1.5% non-uniformity along both the shower direction and the beam direction with these masks in place [6].

When mounted, each module is rotated by 2.5° in the azimuthal plane so that the plane of the wavelength shifter plates does not contain the ep beam axis.

2.2. Readout electronics

One of the important goals of the test beam effort was to gain experience with the final calorimeter readout chain planned for the ZEUS experiment. Many of the novel features of the readout were tested in a data-taking environment before HERA began colliding beams.

An overview of the readout scheme is presented in fig. 2. The readout for the calorimeter is physically split into "Analog Cards", which mount onto the calorimeter, and "Digital Cards" located outside the detector in VME crates. The readout control for the entire calorimeter is administered centrally by a single set of NIM modules. More information on the readout can be found in ref. [7].

The Analog Card integrates and shapes the PMT signals on separate high and low gain scales, samples the shaped signals every 96 ns, delays the signals in analog switched capacitor pipelines, and, when triggered, stores the desired samples from the pipelines in a one event buffer (also a switched capacitor array) before multiplexing them to the Digital Card. The pulse shape at the output of the shaper is shown in fig. 3, along with some of the nominal sampling times, t_i, and the corresponding samples, h_i. Up to eight samples can be stored for every trigger. In this experiment, the eight samples were named h_{-3} to h_4. The two largest samples are h_1 and h_2, and $h_1 \simeq h_2$. The first sample, h_{-3}, is the level of the baseline and has to be

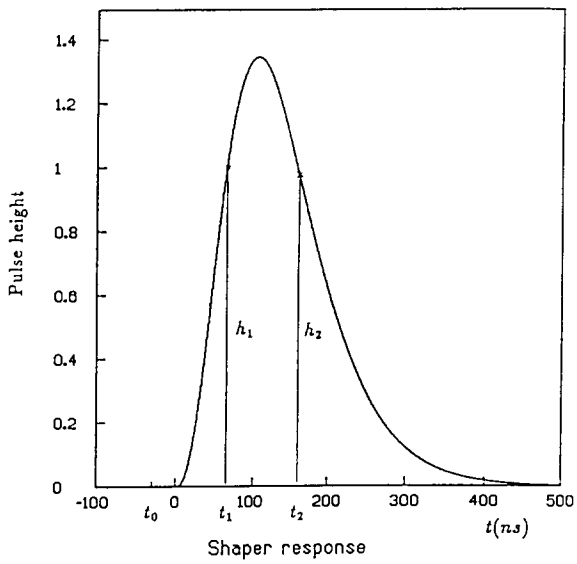

Fig. 3 Pulse shape at the output of the shaper. The pulse is sampled at eight nominal sampling times, t_{-3} to t_4, spaced 96 ns apart. Sampling times t_1 and t_2 and the corresponding samples, h_1 and h_2 are shown.

subtracted from the rest of the samples as described in section 4.4.1. In addition to the pulse shaping and sampling, a dc integration of the DU current is provided as well as analog sums of PMT signals for the ZEUS trigger system. A precision charge injection circuit is provided at the input to each channel for calibration purposes.

The Digital Card digitizes the samples and stores them in a 16 event deep input dual-port memory. The on-board digital signal processor (DSP) then decides between the high and low gain signals; applies all calibration constants related to the electronics; and calculates the energy, time, and other quantities. The calculated values are then stored in a 16 event deep output dual-port memory. Each Digital Card processes signals from 24 phototubes (each with high and low gain readout scale).

During the data taking at Fermilab, calibration constants were applied off-line, and the DSPs were used only for data formatting. For electronics calibration runs, the DSPs calculated averages and root-mean-square values of all the digitized data, reducing the calibration time by two orders of magnitude.

2.3. Photomultipliers, bases, and high voltage readout

The BCAL optical readout system uses Hamamatsu R580 photomultiplier tubes (PMTs), with 162 PMTs per BCAL module all of which were tested before installation on the modules. The averaged quantum efficiency was measured to be 15% at a wavelength of

520 nm. The gain of the PMTs is $\sim 6 \times 10^5$ at the nominal operating voltage of 1300 V and the dark current is less than 1.5 nA.

The PMT high voltage control system consists of 162 Cockcroft–Walton (CW) bases controlled through a single station Ethernet HV controller. The operational principles of the system are briefly described here; a detailed description of the CW PMT base and Ethernet HV controller can be found in ref. [8]. The base design provides for low heat dissipation (0.12 W) and low input voltage. The CW circuit is used to step up the 24 V dc input voltage to the desired high voltage. The voltage division for the PMT dynodes is quantized due to the CW accelerator chain, and so the dynode voltages cannot be set to arbitrary values. The linearity range of the R580 PMT provided by the particular voltage division of this CW base is within 1% up to anode currents of 160 mA at 1300 V. The rms noise level of the CW base is 1.4×10^{-14} C integrated over 400 ns, which corresponds to about 1% of the energy deposited in the calorimeter by a minimum ionizing particle.

An Ethernet HV controller station consists of one CPU card and six analogue controller cards, each controlling 32 bases. Thus, one station can control up to 192 bases; of these, only 162 channels are used. Ethernet was used for communication between the CPU card and an on-line computer, with the trivial file transfer protocol (tftp) used in Ethernet software. The high voltages of PMTs on a module were set by simply downloading, in a predefined sequence, a table containing the 192 high voltage values for the 192 possible HV controller channels. Similarly, reading back the high voltages from a module was performed by transferring a table from the HV controller to the on-line computer. An RS232 communication channel is also available on the computer card, installed for initial testing of the HV controller before the Ethernet became functional.

2.4. Laser

The laser calibration system delivered light pulses to the individual PMTs on the BCAL module by means of optical fibers. The main components of the system included a Laser Science nitrogen laser, a dye cell, neutral density filters, intensity monitors, and the optical fanout system. Triggering of the laser was computer controlled and could be set to be synchronous or asynchronous with the readout electronics clock. Light from the laser (337 nm) was shifted to blue (425 nm) by the dye cell, and then passed through two neutral density filters with twenty attenuation settings, also under computer control, and focused onto a 1-to-2 splitter. About 85% of the light was transported to the test modules via a 35 m long glass fiber while the remainder was provided to the intensity monitors. The fanout on each module used two 1-to-111 commercially built splitters, each supplying the 81 PMTs on one side of one module. Light from the long fiber could be split to feed all four modules on the experimental stand simultaneously or as little as a single half module as desired.

The laser monitors consisted of a 1-to-2 splitter which transmitted light to two wavelength-shifter transition pieces each coupled to a Hamamatsu R580 PMT. The signals from the PMTs were readout using CAMAC ADC and TDC modules. Monitoring of the intensity was necessary because of the $\sim 15\%$ fluctuations in light intensity from pulse to pulse. The TDC module was also used to measure the timing of the laser pulse with respect to the 96 ns pipeline clock.

3. Experimental apparatus

The experimental setup is shown in fig. 4. The modules under study were installed on two stands, the "θ–ϕ" stand and the "muon stand", which were separated by two CCFR target modules [9] serving as the backing calorimeter (BAC) for the modules on the θ–ϕ stand and as a muon filter for the module on the muon stand. A conventional magnetic spectrometer consisting of three dipole magnets (M1, M2, M3), scintillator counters and drift chambers defined the particle tracks and momenta. Particle identification was performed by the backing calorimeter, Cherenkov counters (C1, C2), and transition radiation detectors (TRD). In the fol-

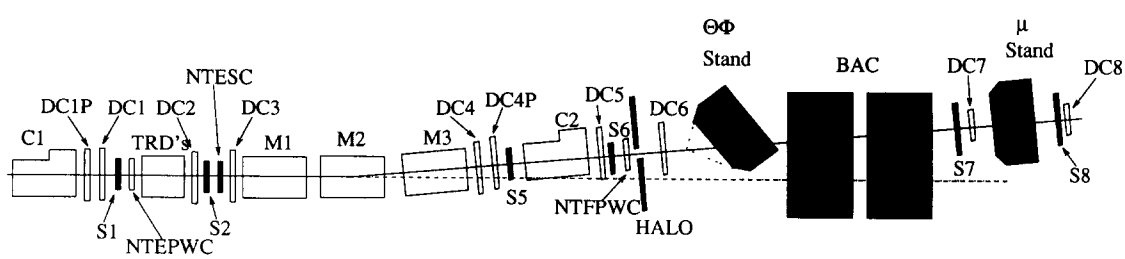

Fig. 4. Layout of experiment E790 apparatus in the Fermilab NT beam line.

lowing, each of these detector elements is described.

In the coordinate system that was adopted in this experiment, the beam defined the positive z-axis, while the positive y-axis was vertical upwards, and the x-axis was horizontal so as to form a right-handed Cartesian coordinate system. Rotations in the x–z and y–z planes corresponded to rotations in the ZEUS frame θ and ϕ directions respectively.

3.1. Beam

The NT (neutrino test) beamline at Fermilab was used to calibrate the modules. Typically 3×10^{11} protons of 800 GeV/c struck a Be target in the 23 s extraction period during each Tevatron cycle of 60 s. A secondary beam of negatively charged particles was momentum selected; data were taken for settings between 4 and 110 GeV/c. The beam consisted predominantly of pions but had typically 1 to 3% electrons, 3% muons and about 5% antiprotons depending on the momentum setting. The beamline contained dipoles that allowed selection of the production angle and beam momentum, quadrupole magnets for focussing, and collimators to adjust the beam rate and remove off-momentum particles.

3.2. Spectrometer

3.2.1. Dipole field

Three dipole magnets, connected in series, provided the necessary field for momentum measurements, bending the beam by 27 mrad. The magnet gap had a cross-section 5 cm $\times$ 28 cm and was 3 m long. The magnet current was read for each spill cycle using a high precision (1%) shunt resistor. Two field mapping measurements taken in 1987 and 1991 gave results consistent within 0.5%. The conversion factors from current to momentum and from field to momentum were about 10 A/GeV and 100 G/GeV respectively, and the remnant field was measured to be 15 G. During the 1991 running period a 10 m long helium bag was inserted into the magnets to reduce the material traversed by beam particles.

3.2.2. Scintillator counters

An array of scintillator counters was used to provide signals for the trigger decision. Each signal was produced by either a single counter or by a double counter in coincidence. The aperture-defining scintillators for the spectrometer magnets were S2 and S5 (see fig. 4). S2 consisted of a pair of overlapping 5.08 $\times$ 5.08 cm^2 scintillator paddles with one photomultiplier tube attached via a light guide to each paddle. S5 was constructed and used in a similar fashion. Several other scintillator counters (S1, S6, S7, S8, and the HALO counter) defined the path of the particles. The HALO counter was a 150 $\times$ 150 cm^2 scintillation counter with a 5 cm square hole in its middle, viewed by two PMTs located on diagonal corners of the scintillator. An "OR" of the signals from either PMT was used in anticoincidence.

3.2.3. Drift chambers

Track positions were measured using an array of ten drift chambers. Four chambers were positioned upstream of the magnets, with a distance between the first and the fourth of about 3 m; four more were placed downstream of the magnets with a distance of about 12 m between the first and the last. The final two chambers were placed on either side of the muon stand. In the first year of running there were five drift chambers. To improve the track reconstruction efficiency, the system was upgraded with five more chambers for the second running.

Eight of the chambers each contained two planes of horizontal wires and two planes of vertical wires. To remove the right–left uncertainty, the wires in alternate planes were offset by 0.75 cm. The dimensions of each chamber were 15.0 $\times$ 15.0 cm^2. The two chambers placed at the muon stand were twice as large in each dimension. The drift chambers were read out with the TRANSPORT TDCs designed for the CCFR neutrino experiment [10]. The drift chamber resolutions were typically 200 μm.

3.3. Cherenkov counters

The beamline contained two Pruss-type Cherenkov counters [11], C1 and C2, which were used to identify antiprotons. Each of the counters had two PMTs, A and B, and had computer-controlled gas flow, pumping, and pressure readout. The broadening of the beam spot by the time it reaches the downstream counter, due to the bending in the intervening dipole magnets, results in the measurements in that counter being less precise.

High gain PMTs with quartz windows, capable of resolving single photoelectrons, were used to collect the Cherenkov light. The accidental rate (i.e. the rate at which noise in the phototubes generated a signal coinciding with the experiment trigger) was measured to be less than 0.3% for all four phototubes.

Pressure curves were taken at 30, 50, and 70 GeV for each counter. Fig. 5 shows the pressure curves at 50 GeV for each PMT in the upstream counter. PMT B collects light emitted at angles less than 5 mrad with respect to the particle direction and PMT A collects light emitted at larger angles. Thus PMT B isolates the various particles while PMT A detects photons radiated from all particles provided it was radiated at an angle higher than 5 mrad.

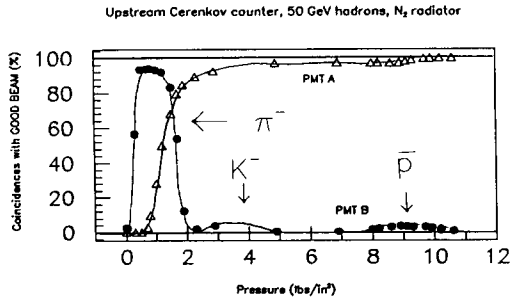

Fig. 5. Pressure curve taken with the Cherenkov counters. The π^-, K^-, and $\bar{p}$ peaks are clearly visible.

The pion, kaon, and antiproton peaks are visible. The antiprotons were measured to constitute about 5% of the beam.

3.4. Transition radiation detectors

Electron identification was performed using a modular transition radiation detector (TRD), with six radiator-chamber modules specifically built for E790 [12]. A typical module can be seen in fig. 6(a). The basic unit consists of a stack of radiator foils flushed with helium. The radiator was followed by a proportional wire chamber filled with a gas containing 90% xenon. The 125 mm space between the chamber windows and the outer cathodes was filled with nitrogen to avoid helium leaking into the chamber volume and so changing the gain. The three gas volumes were held at equal pressure to keep the chamber cathodes flat and thus ensure a uniform gain across the planes.

The cluster counting method was employed to provide the electron trigger. The 64 wires per plane were added in sets of four and subsequently input to a

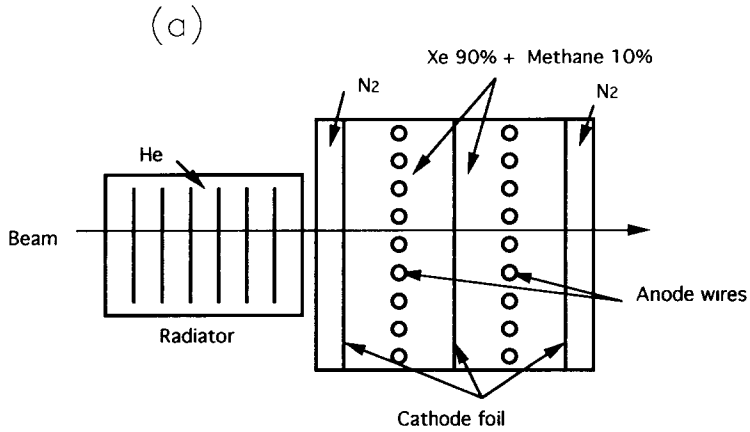

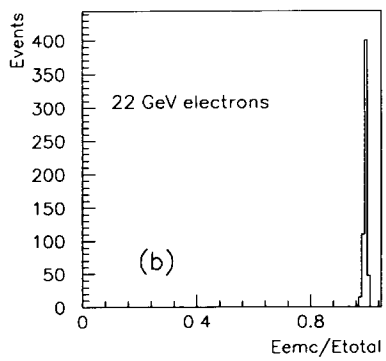

Fig. 6. (a) Typical TRD module. (b) $E_{\mathrm{EMC}}/E_{\mathrm{total}}$ plot at 22 GeV. The fraction of entries in the peak around 1 shows the purity of the electron sample provided by the TRDs.

common base low noise preamplifier. The 16 preamplified signals were sent on short coaxial ribbon cables to amplifier–shaper–discriminator (ASD) cards where the gains and discriminator levels were adjusted.

The purity of the electron samples triggered using the TRD was close to 100%. The electron identification could be independently checked using the fraction of the total energy which was deposited in the EMC section of the BCAL modules, $E_{\mathrm{EMC}}/E_{\mathrm{total}}$. A typical $E_{\mathrm{EMC}}/E_{\mathrm{total}}$ distribution for 22 GeV/c electrons is shown in fig. 6(b); the purity is in excess of 99.8%.

3.5. Mechanical support

Mounting of the BCAL module for the beam tests required mechanical support structures with precise computer controlled motion and position readback.

To fully contain hadronic showers in the BCAL, it was necessary to mount at least three modules, each weighing 10 tons. Furthermore, since the electromagnetic towers are projective this stand should have the ability to rotate about the HERA "interaction point" in both the θ and ϕ directions. The modules should also have a rotation of 2.5° in the x–y plane so that particles from the interaction point cannot escape undetected through the cracks between modules. For calibration using incident muons no adjacent modules were necessary. However, for the nonprojective BCAL HAC towers, the vertical and horizontal translational motion of the stand was desirable. it was decided to construct two stands; a "θ–ϕ stand" holding up to four calorimeter modules, and a "muon stand" holding only one module.

The θ–ϕ stand was designed to emulate one octant of the BCAL calorimeter with beam particles appearing to originate from the nominal ZEUS interaction point. The range of motion allowed the beam to impinge anywhere within the middle two modules, with the lower and upper modules providing additional shower containment. The horizontal motion had sufficient range to allow the beam to impinge onto each of the 53 EMC towers.

The muon stand comprised a moveable cart which carried one module, mounted horizontally. The cart rode horizontally on large box beams and could move vertically to span the full front face width of a HAC1 tower. The horizontal motion allowed each of the 14 HAC towers of the module to be positioned in the beam path.

All motors could be operated in either manual or computer-controlled modes. A computer interface using an RS-422 serial interface to a VME-based microprocessor was available to provide automatic control. The stand position could be set to a precision of 0.1–0.2 mm. To ensure reproducibility of the data, each motion had a zero point defined by a machined step and sensed by a limit switch. The zero point could be reproduced to within 0.1–0.2 mm.

3.6. Backing calorimeter

Two of the CCFR target calorimeter modules (carts) [9] were used as the backing calorimeter (BAC) to catch the longitudinal energy leakage from the BCAL modules placed on the θ–ϕ stand. The upstream cart used iron–liquid scintillator layers in fourteen sampling planes, with 10 cm of iron per plane. Each scintillator plane had wavelength shifter bars along the sides which were viewed by a PMT in each corner. The last five planes of the downstream cart were activated to identify muons.

Calibration of each sampling plane of the BAC was performed by placing a ^{60}Co source at the center of the plane and requiring that, after subtraction of the dark current, the outputs of the four PMTs be the same. Intercalibration of different sampling planes was done with beam muons. The CCFR procedure was followed to define the truncated mean of the summed muon signals from the four PMTs as the mip signal of the sampling plane. The CCFR collaboration had used known energy beams to measure the mip to GeV conversion factor of 0.211 GeV/mip for hadrons [9]. The BAC energy calibration was cross checked with the beam spectrometer and the result agreed to within 1% in the energy range between 20 and 100 GeV. The BAC energy-resolution was also in good agreement with the previous measurements.

3.7. Trigger

The beam contained an admixture of negative pions, electrons, muons, kaons, and antiprotons. The trigger was configured to select particles that satisfied the geometry and optics of the magnetic spectrometer and to reject particles from the beam halo. The various systems participating in the trigger can be seen in fig. 4. Scintillation counters S1, S2, S5, S6, and HALO were used to define the path through the beam optics. Particles which were in time with the Tevatron 18.6 ns clock, and which satisfied $\mathrm{S1} \cdot \mathrm{S2} \cdot \mathrm{S5} \cdot \mathrm{S6} \cdot \overline{\mathrm{HALO}}$ were called "good beam" particles (GB). In the early stages of the experiment two additional pairs of overlapping scintillator paddles (S3, S4) were inserted in the gaps between the spectrometer magnets and also required in the definition of GB. The GB signal was used to define the absolute time of all triggers.

Electrons were identified using the six TRD modules. Typically, a coincidence of hits in at least two TRD modules was needed to identify electrons.

$$\mathrm{Electron} = \mathrm{GB} \cdot \mathrm{TRD}$$

Beam muons were identified by requiring coincidence among a sub set of the scintillators of the BAC and two 20×20 cm^2 single scintillation counters S7 and S8.

$$\text{Muon} = \text{GB} \cdot \text{BAC} \cdot \text{S7} \cdot \text{S8}$$

The Cherenkov counters C1 and C2 were used to identify antiprotons.

$$\text{Antiproton} = \text{GB} \cdot (\overline{\text{C1}} \cdot \overline{\text{C2}})$$

Pions were identified as GB particles that were not in coincidence with TRD, or $\overline{\text{C1}} \cdot \overline{\text{C2}}$, or BAC.

$$\text{Pion} = \text{GB} \cdot (\overline{\text{TRD}} + \text{C1} \cdot \text{C2} + \overline{\text{BAC}})$$

The trigger system was designed such that the absolute timing did not change if any individual component such as scintillators, TRDs etc. was added or removed. This allowed changes to the trigger definition to be made quickly and reproducibly. Signals from the TRD had a time jitter because of the drift time. A wide gate generated from the TRD signal was used to form the coincidence signal with GB.

The Tevatron 18.6 ns rf microstructure allowed, by counting down the rf clock, operation of the trigger and BCAL readout electronics with a 93 ns clock. This mode closely approximated the HERA bunch-crossing period of 96 ns, enabling the calorimeter readout electronics to operate under conditions similar to those at HERA. Since, however, it rendered 80% of the beam useless, this mode was used only in selected runs. For most runs, all rf buckets were used; this was possible because the trigger rate was far below the rate expected at HERA.

3.8. Data acquisition

For each beam related trigger, information was obtained as follows: uncorrected samples and other calorimeter readout information from the digital cards, TDC information from the drift chambers and TRD system, and the phase time of the trigger relative to the calorimeter readout pipeline clock. A bank of CAMAC scalers and other devices also recorded beamline related information, such as number of single and coincidence hits in the various trigger elements, overall trigger statistics, and the value of the spectrometer magnet current. After each spill, an event record was formed containing the data discussed above together with a measurement of the PMT HV readback values; the positions of the fixtures; and a timestamp. An automatic sequence of test triggers (10 laser and 10 DU/pedestal triggers) was performed at this time.

The standard ZEUS calorimeter "Two-transputer" modules [13] (2tp) were used as the VME crate processors. A central 2tp built the full events by gathering the data from all relevant sources and formatting them into ZEBRA banks to form the final event records. The events were then passed to a large 2tp-based ring buffer, which took advantage of the $\approx 50\%$ duty cycle of the accelerator, and up to a VAX system via a commercial transputer interface.

The VAX system consisted of a local cluster of workstations. Data were monitored extensively on-line and simultaneously written to 8 mm Exabyte tape for storage. The VAX system also provided the platform for the run control system and most of the off-line data analysis. The run control system performed automatic sequencing of various run types, driven by programmable lists of fixture positions and readout configurations. The run control was interfaced to all configuration and control tasks in the experiment.

The I/O was limited in various aspects by the commercial transputer interface, the disk and tape transfers, and the VAX system overhead, resulting in a maximum sustainable transfer rate to tape of about 140 kB/s. The size of the events depended on the trigger type. For hadrons, the PMTs from all four BCAL modules and the BAC produced 35 kB per event. For electrons and muons only two to three digital cards were read out, corresponding to 2–3 kB per event. The size of the events for the BAC only was about 4 kB.

4. Experimental procedures

The general procedures for data taking and reconstruction are now described. These include beam optimization, calibration of the readout electronics, setting of the PMT gains, and on-line analysis and monitoring of the data quality.

4.1. Beam optimization

The beam rates and particle compositions at a given momentum were optimized by varying the production angle of the secondary beam. For a given momentum setting the magnet currents were adjusted to optimize the rate at the magnetic spectrometer. Typically about 2×10^5 particles traversed the magnetic spectrometer each Tevatron cycle. The full width at half maximum of a typical momentum distribution for true particles was $\Delta p/p = 1\%$.

Electrons lose more energy than pions in the material in the beamline upstream of the magnetic spectrometer. The fraction of beam electrons could be enhanced by setting the spectrometer at a momentum slightly below that of the NT beamline. For example, although at the nominal settings for 50 GeV/c the electron fraction is only 1%, when the spectrometer was lowered to 40 GeV/c the electron fraction increased to 5%.

4.2. Tracking and momentum determination

The bend angle, and therefore the momentum, was obtained for each event by minimizing an appropriate function of the chamber hits. For the x–z plane, this function is expressed in terms of the hits, x_i, at chambers in the longitudinal coordinate, z_i, and is given by:

$$\psi_x^2 = \frac{1}{N_x^u + N_x^d}\left[\sum_{i=1}^{N_x^u}\left[x_i - (\alpha_u z_i - \beta_u)\right]^2 + \sum_{j=1}^{N_x^d}\left[x_j - (\alpha_d z_j - \beta_d)\right]^2\right], \quad (1)$$

where N_x^u and N_x^d are the number of chambers with hits upstream and downstream of the dipoles, respectively. The minimization is subject to the constraint, $\alpha_u z_0 + \beta_u = \alpha_d z_0 + \beta_d$.

In the equations above, α_u, β_u, parametrize the incident angle of the particle upstream of the dipoles, while α_d and β_d describe the downstream angle. The index i runs over the number of upstream drift chambers, and j over the downstream drift chambers. Here, z_0 is the z coordinate of the bending point of the track in the dipole magnets. Corresponding relations hold for the y–z projection.

Particles with large ψ^2 were rejected. For muons or pions, the cut $\psi^2 < 0.1$ was sufficient to reject badly measured particles. In the case of electrons, a tighter criterion, $\psi^2 < 0.05$ was needed, mainly because electrons have a broader distribution of energy loss when they pass through material.

The positions of all elements in the spectrometer were surveyed, and the beam was used to make a final precision alignment of the chambers. The momentum distribution at every nominal beam momentum setting

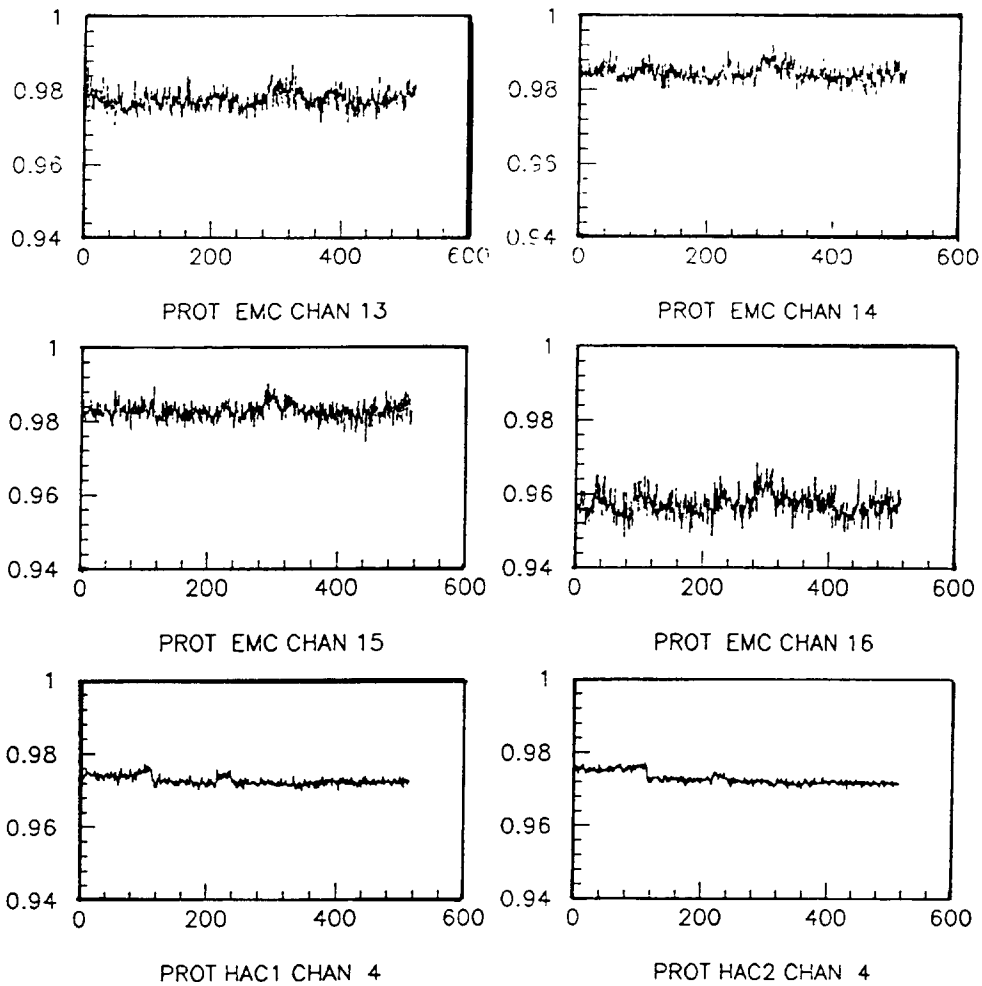

Fig. 7 The ratio of the measured DU current after the first setting to the nominal values versus spill number over a reconstructed 40 h period. The upper four figures present EMC towers 13 to 16, while the lower left plot is the HAC1 tower 4 and the lower right plot is the HAC2 tower 4. The spread of the measurements results from the statistical accuracy of the measurements.

could be reconstructed with $\Delta p/p = 1\%$. Given a finite beam momentum spread, the momentum resolution was less than 1%. The momentum resolution was also estimated independently by fitting separately the drift chamber hits before and after the dipoles, and comparing the projections of these tracks extrapolated to a plane in the middle of the dipole. This method yielded a momentum resolution of about 0.6%.

The absolute scale of the spectrometer momentum calibration was accurate to 1.0%. To estimate the accuracy, the undeflected beam direction was measured by removing the dipoles. The bend angle was then measured from the difference in x between the deflected and undeflected beams as measured with a large drift chamber. Other factors affecting this accuracy were the spectrometer dipole long-term stability, the readout accuracy of the dipole current, the remnant field, and the good field region in the magnets.

4.3. PMT gain settings

The DU induced current from the calorimeter was used to set the gains of the PMTs. The DU current was set to the predetermined values of 133 nA for the EMC, 712 nA for the HAC1, and 908 nA for the HAC2, the values reflecting differences in size among the various sections of the BCAL modules.

The PMT gains were set within 1% of their desired values as follows. The PMT gain, G, as a function of high voltage, V, can be expressed by

$$G = aV^b. \tag{2}$$

The two constants, a and b, were measured for each PMT by measuring the DU currents at seven different high voltage settings, from 950 V up to 1550 V. The value of b was found to be about 7 for all tubes. The high voltage necessary to obtain the appropriate DU current was calculated for each PMT using eq. (2). After resetting the HV controller with these settings, the DU values were found to be within 2–3% of the nominal value. The DU currents were then measured again and a fine adjustment of the PMT gain was calculated using,

$$b\frac{\delta V}{V} = \frac{\delta G}{G}. \tag{3}$$

A new table of high voltage values was prepared and downloaded to the HV controller which yielded DU values typically within 1% of the nominal values.

The PMT gains were quite stable. Typical gain variations versus time are shown in fig. 7, where the ratio of measured DU current to the nominal value is plotted versus spill number. These measurements were taken after the first setting, and they are 1 to 4% away from the nominal values. The PMT gains stayed within 1% during the 40 h period shown. The PMT gains for each module were set after the module was placed on the test stand, and then monitored continuously by reading out the DU currents between spills.

The temperature dependence of the PMT gains was also studied. The change in the gains was 0.2% for each degree (°C) of change in temperature, about half of which was due to temperature dependence of the high voltage system.

4.4. Front end electronics

4.4.1. Charge and time reconstruction

The raw pulse samples must be corrected for differences in the pedestals and gains of individual pipeline and buffer cells. These corrections generate the bulk of the calibration constants [14]. The charge reconstruction produces a normalized charge, with all channel dependent electronics effects removed. The sample values h_i, as defined in section 2.2, are corrected for pedestals and gains, after which the baseline correction is applied. This is done by subtracting sample h_{-3} from the other samples;

$$h_1 \to h_1 - h_{-3}, \tag{4}$$

$$h_2 \to h_2 - h_{-3}. \tag{5}$$

Two quantities relating to the charge, H', and sampling time, T', are then defined by:

$$H' = h_1 + R \cdot h_2, \tag{6}$$

$$T' = (h_1 - h_2)/H', \tag{7}$$

where R is a constant and h_i is the pedestal, gain and baseline corrected value for sample i. The value of H' depends on the positions of h_1 and h_2 on the pulse as is evident from fig. 3. A nominal sampling time $T' = 0$ ns is defined when $h_1 = h_2$. Sampling times can vary for several reasons including different PMT transit times, different cable signal and clock lengths, differences in the time profile of showers according to particle type, and differences in pipeline sampling delays. It is important to correct H' for sampling time differences. The form of the correction depends on the pulse shape, which in turn depends on the type of signal being measured. It was chosen to fix R for all channels and for all types of runs ($R = 1.80$) to approximate the ratio of the slopes at h_1 and h_2 of the shaped pulse, and to correct for the effects of varying sampling times with a polynomial of the form

$$H = H'\left(1 + \sum_{n=1}^{4} c_n T'^n\right). \tag{8}$$

The constants c_n were not measured as part of a normal electronics calibration run. Rather, they were derived separately for different event types which could be expected to have slightly different pulse shapes, namely beam, laser, and charge injector data. A single

set of constants c_n was found to be valid for all channels for a given event type.

Once the dependence on the sampling time has been removed, the relationship between H and Q can be calculated for each channel. This is done using the charge injector by pulsing at several different amplitudes. A linear expression was used to relate the reconstructed amplitude H to the input charge Q:

$$Q = a + bH. \tag{9}$$

The constant a is present only to take into account a small offset in the charge injector pulse. it is not used to reconstruct charge for any other type of event. A simple linear relationship is adequate since the electronic nonlinearities have been measured to be at the $\leq 0.2\%$ level. The ratio of the high to low gain scales is simply given by $b_{\text{low}}/b_{\text{high}}$ and is about 22.

4.4.2. Time measurement

The sampling time is the difference between the time at which the pulse was sampled and the time which would have given $h_1 = h_2$. Given the complicated pulse shape and the need to provide simple algorithms for the DSP, a polynomial function was chosen to reconstruct this time T to sufficient accuracy:

$$T = \sum_{n=1}^{3} d_n T'^n. \tag{10}$$

The constants d_n depend on the event type as described in the previous section. T is related to the sampled points on the pulse, and is not the event time. To calculate the time of the event, t, a correction has to be made for the sampling time differences in the different channels. This time offset, T_{offset}, is a channel dependent quantity, and must be calculated separately for different event types. The event time as measured by a single channel is then

$$t = T - T_{\text{offset}}. \tag{11}$$

The overall time of an event can be measured from a weighted channel time sum.

4.4.3. Performance of the calorimeter readout

During data logging, ten pedestal and laser events were taken every minute between beam spills to monitor the functioning of the electronics. Charge injector events were typically logged once per shift in a separate run for later analysis. All calibration constants used for data reconstruction were determined on-line [14], and the extra runs were recorded to tape to monitor the performance of the electronics later.

Random trigger events were taken to determine the pedestal. It was found that the mean energy reconstructed in pedestal events is 0 ± 1 MeV where the error represents the statistical uncertainty of an individual channel. The noise level is given by the rms of the reconstructed energy distribution for pedestal events. It was found to be 8.6, 16.3, 18.0 MeV for EMC, HAC1, and HAC2 channels, respectively, and is completely dominated by the DU radioactivity. The noise between the two PMTs on a single cell is partially correlated so that the resultant cell noise is 14.4, 29.0, and 32.2 MeV for the three calorimeter sections. When the PMT high voltage is turned down to remove the DU contribution to the noise, the electronics noise is found to be 4 MeV per channel.

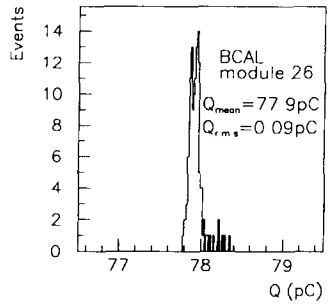

Fig. 8. Reconstructed charge in pC for a charge injector run for all channels of module 26. In this example, the fractional error on the charge reconstruction has an rms of about 0.1%.

Using the charge injector, Q_{inj}, at several settings it was established that the linearity of the charge reconstruction is 0.2%. Fig. 8 shows the reconstructed charge for a high Q_{inj} setting for all channels of module 26. The fractional error on the charge reconstruction has an rms of 0.11%.

4.5. Laser studies

The laser calibration system was designed to perform the following tasks.

- Monitoring the calorimeter long term stability. The DU induced current is expected to change the PMT gain at a level of 1% per month. Long term damage to the scintillator and wavelength-shifter material from beam, DU radiation or from mechanical handling might also cause a reduction in the signal, though this is expected to be small. The laser, together with the DU calibration, can help to differentiate between these causes. For the laser system, the number of photoelectrons produced at the PMT photocathode for a light signal characteristic of a minimum ionizing particle (mip) was monitored. In the absence of an operating laser monitor in this run, changes in one channel relative to its neighbors in the same module were monitored.
- Determination of the linearity of the PMT responses over the full dynamic range.

- Determination of the timing offsets for each PMT channel. Timing information can be used to reject beam-gas and cosmic muon events in the ZEUS environment.

4.5.1. Number of photoelectrons

The total number of photoelectrons, $\mathcal{N}_{pe}$, produced in the PMT by a laser pulse can be estimated from the mean, $\langle Q \rangle$, and rms deviation, σ, of the charge distribution resulting from a single laser run according to the following equation:

$$\mathcal{N}_{pe} = (\langle Q \rangle / \sigma)^2. \tag{12}$$

The number of photoelectrons per GeV, n_{pe}, can be obtained by scaling $\mathcal{N}_{pe}$ from $\langle Q \rangle$ to Q_{GeV}, the average charge given an energy deposition of 1 GeV:

$$n_{pe} = Q_{GeV} \frac{1}{\langle Q \rangle} \mathcal{N}_{pe} = \frac{C}{\alpha} \frac{1}{\langle Q \rangle} \left(\frac{\langle Q \rangle}{\sigma} \right)^2, \tag{13}$$

where the parameter $C = 1.11$ is a correction factor for the effects of photostatistics at subsequent dynodes of the PMT. The value of a was 11.33 pC/GeV at ANL and 11.0 pC/GeV at DESY. The laser amplitude jitter (15%) was removed by normalizing the charge in each channel by the total charge summed over all channels for that event, after removing saturating channels.

The n_{pe} were determined at the time when the modules were assembled at ANL and also at DESY after the transatlantic shipment. The mean n_{pe} were 76.6 ± 20.0 in the EMC and 125.6 ± 33.0 in the HAC for the first measurements and 78.1 ± 19.2 in the EMC and 121.9 ± 26.9 in the HAC for the DESY measurements. The results as a function of module number are plotted in fig. 9, as crosses and open circles respectively.

The parameter n_{pe} is also related to the known gain, G, of the PMT. The gain of a PMT is given by eq. (2). The parameters a and b for each PMT were obtained by fitting the measurements done at the University of Wisconsin [15]. The charge in coulombs produced by 1 GeV of deposited energy, Q_{GeV}, is then given by:

$$Q_{GeV} = G n_{pe} \times 1.6 \times 10^{-19}. \tag{14}$$

All PMTs in a CAL section have been set so as to yield the same value of the DU current. Hence the values of Q_{GeV} and n_{pe} can be calculated for each channel. These calculated values appear as open squares in fig. 9. The agreement among the three measurements is satisfactory.

4.5.2. Timing

Particles impinging on the calorimeter at the same time ($t = 0$) will produce a different measured time in the various channels. These time offsets can be determined by examining the laser response, since light pulses are produced in all channels at the same instant (within 0.5 ns). The phase dependent dimensionless quantity, T', defined in eq. (7), is plotted in fig. 10(a) against the time as measured by a TDC (see section 2.4). The curve was fit to a quadratic function which was used to reconstruct the time offset for each channel. The pulse shape reconstructed from an asyn-

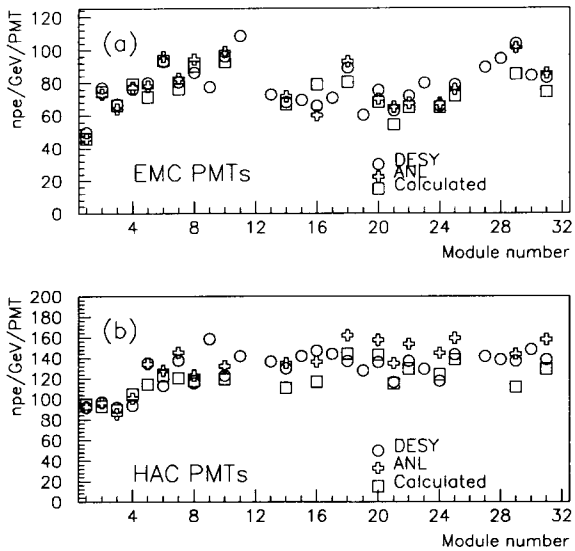

Fig. 9. Number of photoelectrons per GeV per PMT (n_{pe}) as a function of module. (a) EMC towers. (b) HAC towers.

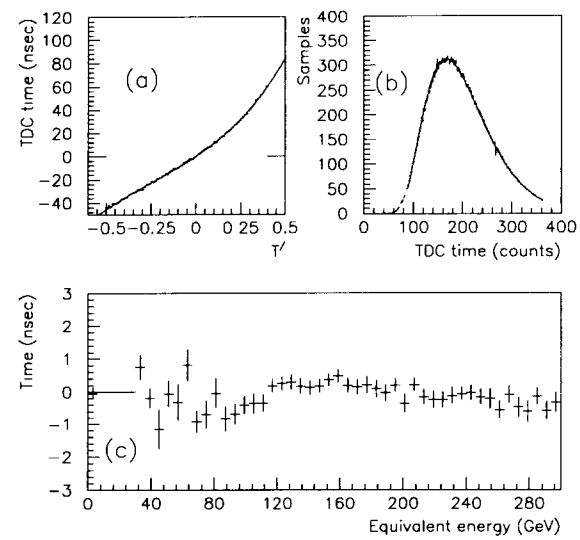

Fig. 10. (a) TDC counts versus T'. The fit is three parameter polynomial. (b) The pulse shape at the output of the shaper could be reconstructed by plotting the samples h_i versus the TDC counts in an asynchronous laser run. (c) Calculated time offsets (ns) versus equivalent energy (GeV).

chronous laser run is shown in fig. 10(b). The time offsets differ by as much as 14 ns from one PMT to another; the rms for a large group of PMTs was about 3%. There were no correlations between time offset and energy from 30 GeV up to 300 GeV, as shown in fig. 10(c).

5. Data analysis and results

In the following sections the results of the data analysis are described. As discussed previously, the beam defined the positive z-axis, while the positive y-axis was vertical upwards, and the x-axis was horizontal so as to form a right-handed Cartesian coordinate system. Rotation angles in the x–z and y–z planes correspond to the ZEUS θ and ϕ angles respectively. The magnitude of θ, and the tower number, increase as one goes from the FCAL direction to the RCAL direction. Particles of normal incidence, with $\theta = 90°$, hit the edge between EMC towers 35 and 36.

To simulate the effects of the ZEUS coil, data were also taken with an aluminum bar having a thickness of $0.87X_0$ placed about 30 cm in front of the calorimeter.

All data were corrected for the channel-to-channel gain variations, normalizing the observed charge to the ratio of nominal to measured DU current values. Ten DU current measurements were taken after each spill for this purpose. To remove non-Gaussian tails of the DU measurement, due to PMT discharges, the highest and lowest values were ignored and the average of the eight remaining values was used.

5.1. Position dependence of the response

Studies were performed to examine the uniformity of response within a tower, as well as the effects of dead material, cracks, etc. Runs were taken (fine scans) with electron and muon triggers, with the beam directed at a sequence of positions distributed over the face of individual towers by moving the θ–ϕ and the muon stands. It was observed that hadron showers do not exhibit local nonuniformities due to their large spatial extent.

5.1.1. Muon results

Because of the high energy Landau fluctuation, the charge corresponding to the energy deposition of a muon (mip) must be defined. In the analysis, the "truncated mean" method was used unless specifically stated otherwise. The "truncated mean energy deposit" is the mean muon response distribution between 20 and 200% of the truncated mean itself. The truncated mean, used because relatively low statistics are needed to determine it well, is about 14% larger than the most probable energy loss for the muon energies used here.

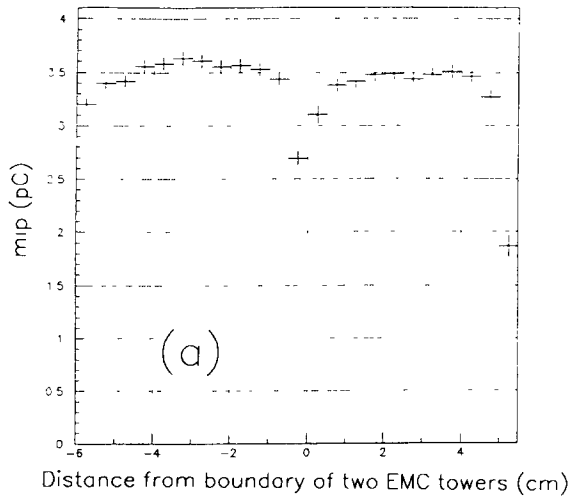

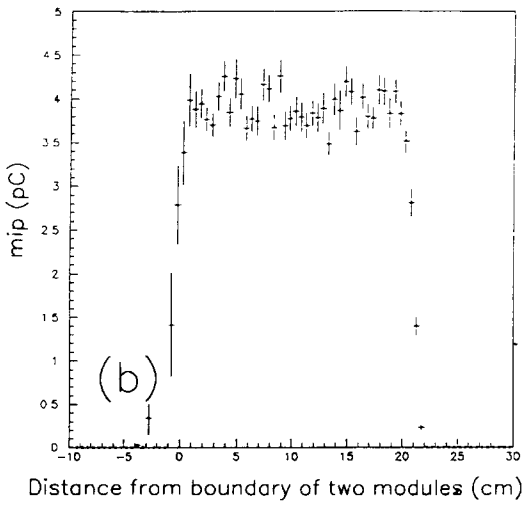

Fig. 11. (a) Collected charge from muons (in pC) as a function of x across EMC towers 19 and 20 of module 8. (b) Collected charge from muons as a function of y across module 8.

Fig. 11a displays this response to muons versus x from a fine scan across the boundary between two EMC towers. The total charge is the sum of both towers. The decrease in response between two towers is caused by the dead space between adjacent scintillator tiles. Fig. 11b shows the response from a fine scan in the y direction across a single module. The rise and fall at the edges of the module are clearly visible. The plateau of the (full) response is about 20 cm in length, the effective width of the module as viewed by the beam.

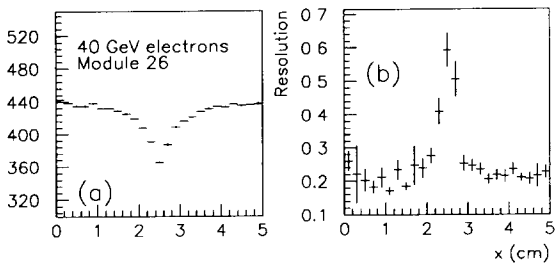

Fig. 12. (a) Collected charge from 40 GeV electrons as a function of x between towers 33 and 34 of module 26. (b) Electromagnetic energy resolution as a function of x between towers 33 and 34 of module 26.

5.1.2. Electrons

Data were collected using the electron trigger and beam optimization at 40 GeV. To further refine the electron sample, the collected charge in HAC2 was required to be less than 50 pC (about 4.5 GeV).

Variation in response in the x direction is expected due to the particle momentum selection and from the calorimeter itself. Particles with different momenta bend by a different amount in the magnetic field and impinge at different x-positions on the front face of the module. The effect of this momentum spread was removed by scaling the reconstructed energy, event-by-event, with the measured beam momentum of that particular particle. The remaining effect can be seen in fig. 12(a), a scan from the midpoint of one tower to the midpoint of the next. The drop in response across the gap between towers 33 and 34 of module 26 is evident. The 10–12% reduction in response for this case is characteristic of all EMC towers.

The shape of the response curve of fig. 12 was parametrized with a four-parameter function of the form:

$$Q = Q_0\left[1 - \left(\frac{x - x_0}{\Lambda}\right)^3\right] \tag{15}$$

with $x - x_0 = 0$ for $|x - x_0| < F$,

and $x - x_0 = |x - x_0| - F$ for $|x - x_0| > F$,

where Q_0 is the maximum response of the tower, x_0 is the position offset from the tower center, Λ is a curvature parameter describing the shape of the response at the edge of the tower, and F is a parameter describing the tower region where the response remains constant.

This function can be used to correct the response to within 1–2% of the value at the center of the tower,

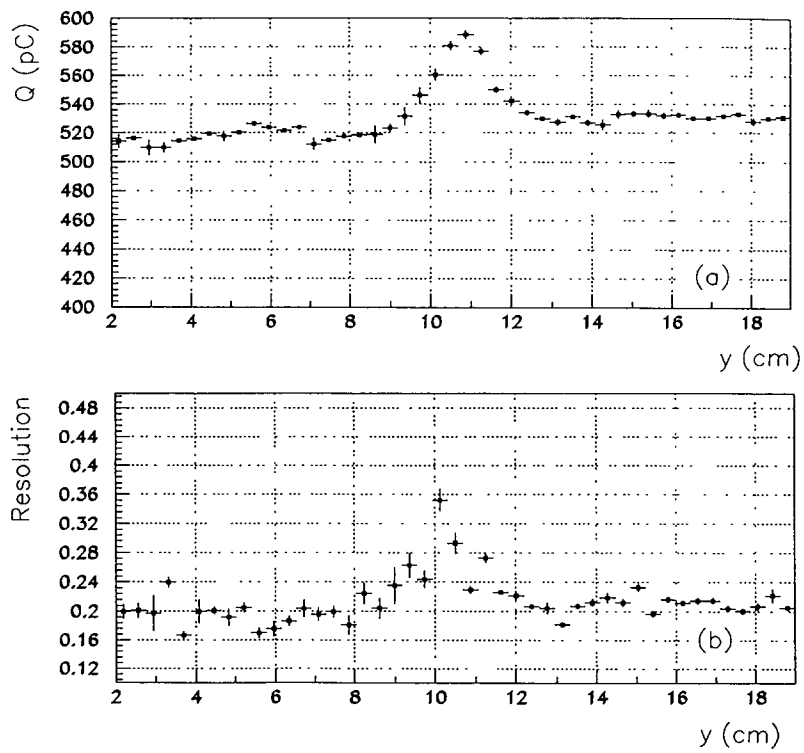

Fig. 13. (a) Collected charge from 40 GeV electrons in the crack between modules 12 and 26, for tower 33. (b) Electromagnetic energy resolution in the crack between modules 12 and 26, for tower 33.

Table 1
HAC tower uniformity results for the 1990 run where 50 GeV muons were used

HAC tower type	BCAL module number	Truncated mean charge (Q)					
		Left PMT		Right PMT		Left + Right PMT	
		Mean [pC]	RMS [%]	Mean [pC]	RMS [%]	Mean [pC]	RMS [%]
HAC1	1	4.32	0.93	4.35	0.84	8.67	0.74
	3	4.45	0.77	4.44	1.20	8.89	0.74
	8	4.34	1.35	4.33	1.12	8.67	1.12
	Avg(1,3,8)	4.37	1.70	4.37	1.55	8.74	1.50
HAC2	1	4.41	1.37	4.46	1.18	8.86	1.06
	3	4 48	0.95	4.47	0.94	8.96	0.83
	8	4.35	3.13	4.39	1.03	8.74	1.60
	Avg(1,3,8)	4 42	2.26	4.44	1.29	8.85	1.53

except in the last 2 mm of the tower where the correction works to only about 3%. In correcting the response for its x dependence, a single set of fit parameters was used for all towers, except for the offsets x_0, which could vary from tower to tower since it depended on the tracking system and not the calorimeter.

In the y direction the total response is seen in fig. 13 to increase at the interface between modules, due to the presence of the wavelength shifters. This effect is partially, but not completely, compensated by inserting 1.6 mm thick lead sheets between BCAL modules. Fig. 13(a) shows the collected charge in the crack between modules 12 and 26, for tower 33. The net effect is again about 10%. In the central towers (33 and 34), the collected charge in the EMC drops between modules, as electrons are able to penetrate further into the calorimeter, while the HAC response increases. In the edge towers (5 and 6), the EMC response fluctuates below and above the mean, while the HAC energy goes up in such a way as to make the overall signal the same as that of the central towers. In summary, everywhere in the calorimeter, the effect of the module interface is to increase the visible energy by about 10%. A lookup table of position versus energy was used to correct the y (the ZEUS ϕ coordinate) dependence. The table corrects the energy to an accuracy of 1 to 2%.

5.2. Tower and module uniformities

Since not all 32 modules of the BCAL could be put into the test beam, the measurement of the uniformity of the response of the various towers and modules is necessary in the estimation of the systematic error at ZEUS. The uniformity of the EMC towers was investigated using both electron and muon triggers. For the HAC towers, only incident muons could be used [16].

5.2.1. HAC tower-to-tower uniformity

Coarse scans, where the beam was aimed at the centers of each of the 14 HAC towers along a module, were used to determine the tower-to-tower uniformity within each module. For each tower, Q was calculated for the left and the right PMTs separately as well as

Table 2
HAC tower uniformity results for the 1991 run where 100 GeV muons were used

HAC tower type	BCAL module number	Truncated mean charge (Q)					
		Left PMT		Right PMT		Left + Right PMT	
		Mean [pC]	RMS [%]	Mean [pC]	RMS [%]	Mean [pC]	RMS [%]
HAC1	12	4.59	0.75	4.60	1.12	9.19	0 85
	26	4.63	0.60	4.69	0.78	9.35	0.64
	32	4.69	1.09	4.78	0.32	9.49	0.64
	Avg(12,26,32)	4.63	1.30	4.69	1.80	9.34	1.47
HAC2	12	4.63	0.62	4.67	0.95	9.33	0.64
	26	4.68	0.83	4.77	1.06	9.47	0 92
	32	4.66	0 99	4.75	0.72	9.43	0.78
	Avg(12,26,32)	4.66	0.89	4.73	1.28	9.41	0 99

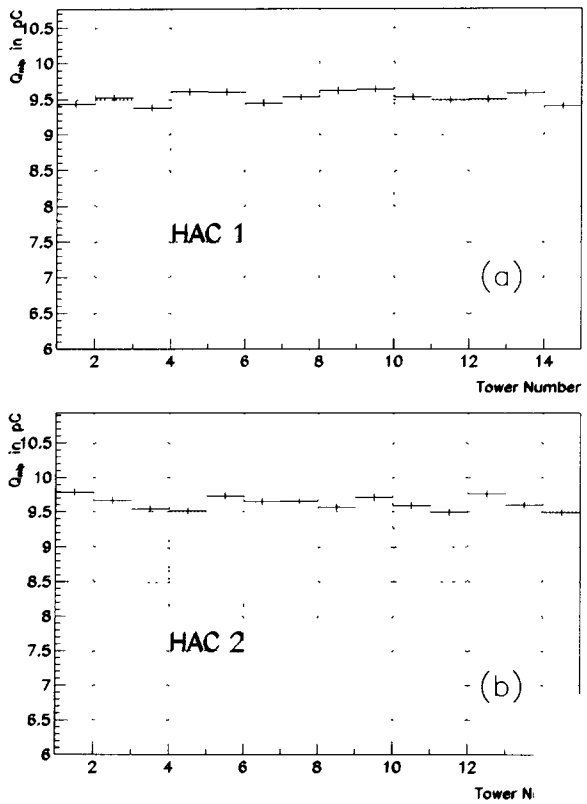

Fig. 14. Truncated mean charges, Q as a function of tower number for a typical module. The errors shown for each tower in the figure are statistical. (a) HAC1. (b) HAC2.

their sum. The rms deviation from the mean of the distributed Q values from the 14 towers was used to characterize the uniformity within a module.

The data for the 1990 run used 50 GeV muons and the 1991 data used 100 GeV muons. The results for the modules tested in the 1990 run are summarized in table 1. Within one module, the responses of the HAC towers were equal to within about 1%, while the module-to-module uniformity was at the 1.5% level. It should be noted that there were some recognized lightleaks in the modules during these tests which were fixed for the 1991 run.

Slightly better uniformities were measured for the three modules (12, 26, and 32) tested in the 1991 run, where the tower-to-tower uniformities were typically 0.7%. The results for the 1991 run are summarized in table 2. Notice that the data for the 1991 run, which used higher energy muons, have higher values of Q.

Figs. 14(a) and 14(b) show Q for HAC1 and HAC2 respectively, as a function of tower number for a typical module. The errors shown for each tower in the figure are statistical.

The module-to-module uniformity is somewhat worse than the tower-to-tower uniformity within a given module. This may be due to minor differences in the construction of the modules which results in slightly different average charges.

5.2.2. EMC tower-to-tower uniformity

5.2.2.1. Electron results. To investigate the tower-to-tower uniformity of the EMC, electron coarse scans, where the beam was aimed at the centers of each of the 53 EMC towers along a module, were performed. A nominal beam momentum of 50 GeV/c was used.

The collected charge for an EMC tower was computed as the sum of the left and right PMTs. The total deposited charge was calculated by adding the contributions of the central tower plus the two adjacent EMC towers on either side. (Note that this implies that the charge could not be reconstructed for the two EMC towers on the ends of the module.)

The selection cuts in the coarse scans with electrons are listed below:

- To remove the remaining pion contamination, $0.95 < E_{\mathrm{EMC}}/E_{\mathrm{total}} < 1.05$ was required. Fig. 6(b) shows a typical $E_{\mathrm{EMC}}/E_{\mathrm{total}}$ distribution for electron triggers.

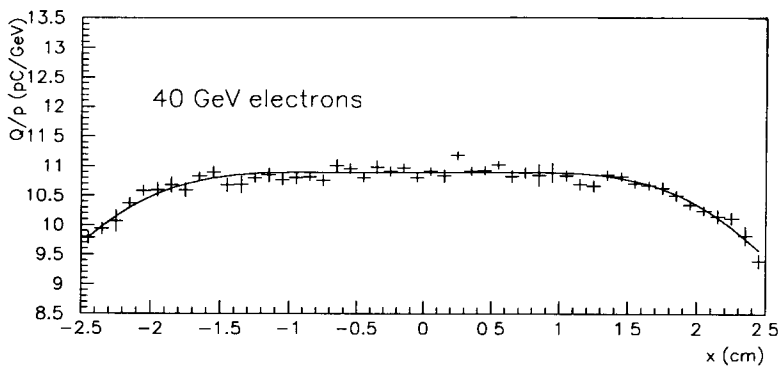

Fig. 15. Collected charge in pC by an EMC tower for 40 GeV electrons as a function of x in cm. The curve is a fit using eq. (15).

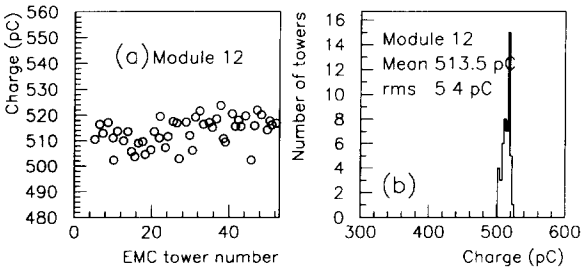

Fig 16. (a) The mean charge measured in each of the EMC towers for BCAL module 12 with 47.6 GeV electrons is plotted versus tower number for data taken without the coil. (b) The projection onto the charge axis shows that the responses of the EMC towers are equal to within 1% (rms)

- The presence of spacers between the scintillator tiles causes a local increase of the amount of inactive material and hence a decrease in the response. As can be seen in fig. 15, the mean response drops by 10% at the edges of an EMC tower. The curve superposed on the plot is a fit with function (15). To exclude regions with reduced response, it was required that the particles hit within ± 1 cm of the center of the tower.

To remove the effect of the beam momentum spread, the deposited charge was scaled by the average beam momentum divided by the measured momentum on an event-by-event basis. The mean charge measured in each of the EMC towers for BCAL module 12 is plotted versus tower number in fig. 16(a) for data taken without the coil. The projection onto the charge axis is shown in fig. 16(b), showing that the responses of the EMC towers are equal to 1% (rms). Data were also taken with the coil in front of the modules, but at a lower beam momentum of 42 GeV/c, where a uniformity of 1.3% was measured for module 12. As summarized in table 3, similar results were obtained also for module 26. In the case of data taking with the coil in place, the collected triggers at every experimental point were only one fourth the number of triggers per point in a run without coil. The reduced statistical precision explains the difference in the measured uniformities. The responses of the two modules are equal within 0.5%.

5.2.2.2. Muon results. The uniformity of the 53-EMC towers of each module was also studied with 50 GeV muons. The beam was centered in the middle of each EMC tower. Approximately 8000 events were collected

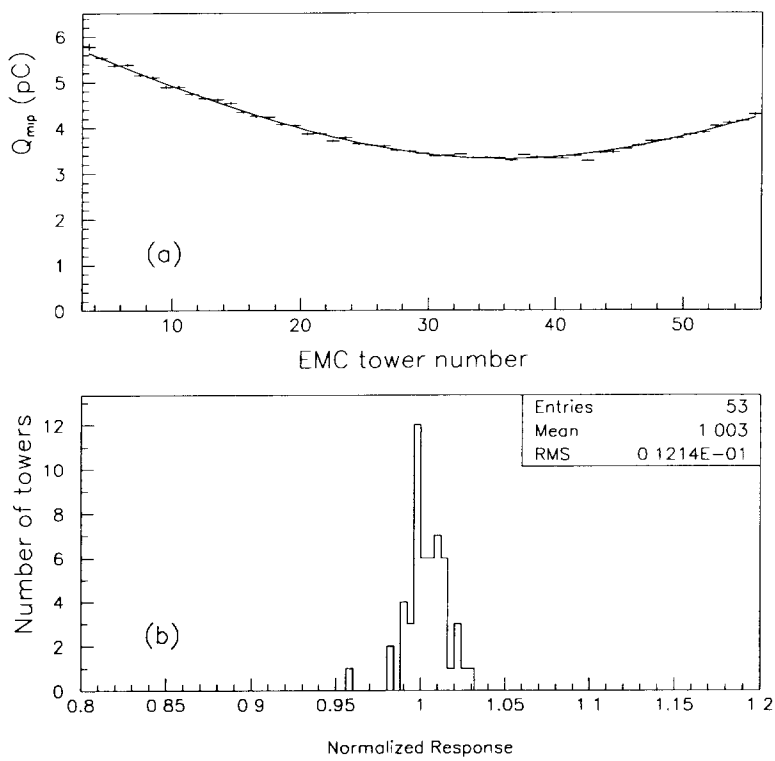

Fig. 17. (a) The DU corrected Q for each of the EMC towers in module 12 taken with 50 GeV muons (b) Distribution of the EMC towers responses after they were normalized to the fit value. The rms deviation, $\simeq 1.2\%$, indicates the non-uniformity.

Table 3
Summary uniformity results. The data with coil were taken with 40 GeV electrons while data without coil were taken at 50 GeV nominal energy. The differences in uniformities can be attributed to differences in statistical precision

Module number	Substitute ZEUS coil			
	OUT		IN	
	Beam energy [GeV]	Uniformity [%]	Beam energy [GeV]	Uniformity [%]
12	47.6	0.97	41.0	1.34
26	47.8	1.05	41.0	1 32
Avg	47.7	1.01	41.0	1.33

per tower to ensure a statistical error of less than 1% after event selection. The following criteria were used for selecting good muon events:

- To remove contamination, the total charge deposited in a tower (two PMTs) was required to lie between 0 and 100 pC.
- The muon was required to hit the center of the EMC tower to within ± 1 cm.

About 2000 events were selected for each tower. The values of Q for each of the EMC towers in module 12 is displayed versus tower number in fig. 17(a). The effective depth of scintillator traversed by a muon varies as a function of θ because of the projective geometry of the EMC towers. Superimposed on fig. 17(a) is a fit with the expected form of $Q = Q_0/\cos(90° - \theta)$, where Q_0 is the response at $\theta = 90°$. The mean response of each tower, normalized by dividing by the fitted curve, is plotted in fig. 17(b). The rms of the distribution indicates the tower-to-tower uniformity is within 1.2% for module 12. As summarized in table 4, similar results were obtained for module 26, where the uniformity is 1.0%. Comparing the data for modules 12 and, 26 shows the average responses, to muons for the two module are equal to within 0.3%.

Table 4
Summary of EMC muon uniformity results taken with 50 GeV muons

Module number	Average charge [pC]	Uniformity [%]
12	3.27	1.2
26	3.26	1.0
Avg	3.27	1.1

5.3. *Absolute calibration, linearity, and energy resolution*

One of the goals of the test beam effort was to measure the absolute calibration of the BCAL response, namely, the conversion from pC of collected charge to GeV of incident particle energy, for DU currents of 133, 712, and 908 nA, for the EMC, HAC1, and HAC2, respectively. For this purpose, and to examine the linearity of the BCAL response versus particle energy as well as the BCAL energy resolution, runs were taken ("energy scans") with beams of varying energies.

5.3.1. *Response to electrons*

5.3.1.1. Absolute response. The absolute response of the calorimeter to electrons was calculated from coarse scans and energy scans, with and without the substitute coil. An analysis of the coarse scans similar to the one applied in the case of the uniformity studies was performed. In all analyses, there has been an event-by-event momentum correction. The results are shown in table 5.

Using the coarse scan data sample, the x coordinate of the accepted particles was selected to be within 1.0 cm from the center of the tower. In this case the response distribution is uniform and effects of spacers are minimized; however, the sample size is reduced by a factor of 2.5 with a consequent increase in the statistical error. The momentum distribution and the

Table 5
Summary of results from electron data analysis. The error displayed for the resolution that was derived from the coarse scans of module 12, is the rms of the resolutions of the EMC towers in one module. The statistics for the coarse scan with coil in were much less than without coil

Module number	Scan type	Coil	Tower number	p_{beam} [GeV/c]	α_e [%]	Response [pC/GeV]
12	coarse	no	All	47.6	19.0 ± 1.7	10.78
12	coarse	yes	All	41.0	20.2 ± 3.2	10.56
26	coarse	no	All	47.8	19.0	10.70
26	coarse	yes	All	41.0	20.2	10.51
12	energy	no	35	6–74	21.0	10.78
12	energy	no	34	6–74	21.2 ± 0.34	10.73 ± 0.006
32	energy	yes	34	8–90	21.1 ± 0.55	10.54 ± 0.013

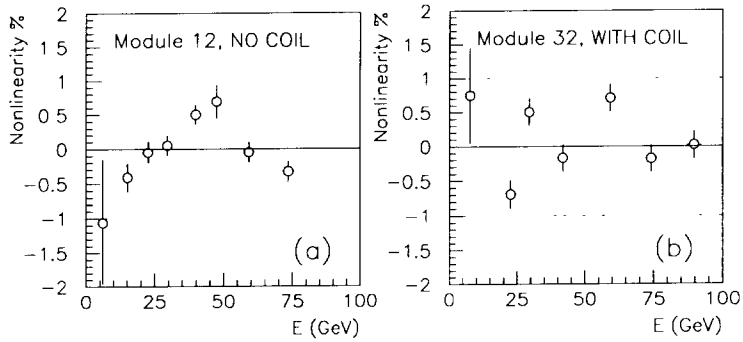

Fig. 18. The measured nonlinearities versus energy for: (a) module 12, no coil and (b) module 32, coil in place.

corresponding collected charge were plotted separately for each beam momentum setting and fitted with Gaussian forms. The mean and deviation of the Gaussian fits agreed well with the simple mean and rms of the distributions, showing that distribution tails are not important.

The energy linearity studies were conducted on modules 12 and 32. The data with module 32 were taken with the substitute coil in place. Electrons of momenta between 7 and 90 GeV/c hitting towers 34 and 35 were used in these studies.

Two alternative methods were used to analyse the data. The first, also used in the coarse scans, involved a straight line fit to the (Q, p) pairs. The slope of the line then gives the absolute calibration in pC/GeV. In the second method, the response to electrons, Q/p, from each beam energy setting was plotted versus x and the distribution was fit to the function (15). The results are summarized in table 5, rows 5 to 7. The statistical error in the absolute response is small compared to the differences in the response values coming from the different methods. The discrepancies, however, are of the same order as the measured uniformity differences among towers and modules (1%). The presence of the coil causes a reduction of the response by 2% over a range of beam energies between 10 and 90 GeV.

5.3.1.2. Nonlinearity. In the nonlinearity studies no x cut was applied to the data, to minimize the statistical error. The response variation as a function of x was fitted with function (15) and the parameter Q_0 was used as the tower charge. The nonlinearity for a given beam energy setting i, NL_i, was defined by:

$$NL_i = \frac{(Q_0/p)_i - (Q_0/p)_g}{(Q_0/p)_g} \times 100, \qquad (16)$$

where $(Q_0/p)_i$ is the response at setting i and $(Q_0/p)_g$ is the global response, derived from either method. The measured nonlinearities versus energy for modules 12 and 32 are plotted in figs. 18(a) and 18(b), respectively. The error bars in the plots show the statistical errors. As can be seen, the nonlinearity is less than 1% over the range investigated.

5.3.1.3. Energy resolution. In the calculation of the energy resolution, an x cut of $|x| < 1.0$ cm was applied to avoid broadening of the distribution because of the dead space between towers.

In the energy scan data samples, the reconstructed charge (Q) distribution for each energy setting was fitted by a Gaussian with mean $\langle Q \rangle$, and standard deviation σ_Q. In fig. 19, the resolution, $\sigma_Q/\langle Q \rangle$, was plotted versus the beam energy E and fitted with the function $\alpha_e/\sqrt{E} + \beta$. It was found, as expected, that $\beta \simeq 0$. The errors on the plot are statistical and were obtained from the Gaussian fits. The results have been summarized in column 6 of table 5. The parameter α_e was found to be 21.1% in the few towers that were studied.

Using coarse scans, $\langle Q \rangle$ and σ_Q were calculated for each EMC tower in a similar fashion. The resolutions of the individual towers were fitted with the form anticipated for sampling fluctuations, $\alpha_e/\sqrt{\cos(\theta - 90°)}$. The results are also summarized in column 6 of table 5.

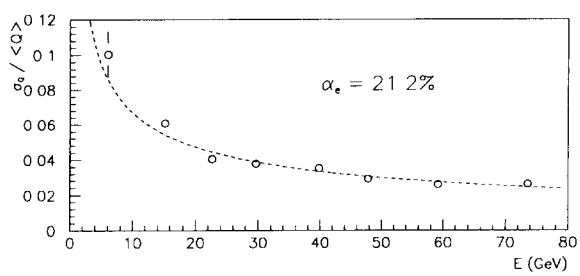

Fig. 19. Relative error of the collected charge as a function of energy. Module 12 data without coil. The dashed line is a fit of the form $\alpha_e/\sqrt{E}$ to the data.

The resolutions calculated for all EMC towers of module 12 were normalized using the fitted curve to the value at normal incidence. The resolution distribution mean and rms was $\alpha_e = (19.0 \pm 1.7)\%$ without coil and $\alpha_e = (20.2 \pm 3.2)\%$ with coil. The rms values include both the error due to statistics and due to differences in resolution between towers, which are small. The rms values are consistent with the statistics of the two sets of data with and without coil.

The fine scan data were also used to calculate the dependence of resolutions across tower and module boundaries. In fig. 12(b), the calculated resolution is plotted versus x in the boundary between towers 33 and 34 of module 26. A degradation from about $20\%/\sqrt{E}$ to $60\%/\sqrt{E}$ is seen. The resolution dependence on the y (ϕ) coordinate across modules 12 and 26 in EMC tower 33 is plotted in fig. 13(b). The effect in this case is a degradation in the resolution to $35\%/\sqrt{E}$. These effects are due to the dead material and empty space between towers or between modules. The effect in the x coordinate is more severe because the EMC towers were exactly projective in this direction for these beam tests. In the y direction the effect is not so pronounced because the modules were installed so that their axis is tilted with respect to the radial axis by 2.5°. Note that the energy resolution at ZEUS is expected to exhibit a reduced variation in the boundary between EMC towers due to the finite extent of the particle bunches in HERA.

5.3.2. Response to hadrons

5.3.2.1. EMC-HAC intercalibration, absolute response. The first step in the hadron analysis is to determine the intercalibration constant between the various calorimeter sections. The two HAC sections are intercalibrated to a precision of 1% from the original DU settings as checked by the muon measurements. The ratio of the DU currents had been chosen according to an estimation of the scintillator area and the effect of the different cladding thicknesses. Beam measurements are necessary to measure the actual intercalibration constants. To intercalibrate the EMC and HAC sections, the energy of the particle i, E_i, is related to the collected charge Q by:

$$E_i = \frac{1}{\alpha_h}\left(Q_{\mathrm{EMC}_i} + \alpha Q_{\mathrm{HAC}_i}\right), \tag{17}$$

where α and α_h are parameters to be determined.

The α parameters were determined after the tower-to-tower and module-to-module uniformities were demonstrated to be 1%, and the absolute beam momentum scale was calibrated with our beam spectrometer and cross-checked with our BAC to a precision of 1%.

To measure the parameters α and α_h, the following formula was used:

$$\chi^2 = \sum \frac{(E_i - P_i)^2}{(0.35)^2 P}, \tag{18}$$

where P_i is the incident momentum of the particle measured from the beam spectrometer, E_i is the reconstructed energy in the calorimeter from eq. (17), and P is the nominal beam momentum. The denominator reflects the assumption that the energy resolution, σ_E/E, of the calorimeter is $35\%/\sqrt{E}$.

If the summation (18) runs over all events at different nominal beam momentum settings, as in an energy scan data sample, the minimization procedure to estimate the α parameters is equivalent to optimizing the linearity of the calorimeter response to hadrons. Minimization of the χ^2 for one nominal beam energy, on the other hand, optimizes the energy resolution at that energy.

In addition to the above data sets, fine scan data collected with the coil in, and coarse scan data at different θ angles without the coil were also used. Note that the fine and coarse scans were taken at a nominal beam energy of 50 GeV. All of these data have been checked to determine the constants and the results are in agreement within 1 to 3%.

To select good events, the following selections were applied.

- $Q_{\mathrm{EMC}}/Q_{\mathrm{total}} < 0.96$, to eliminate electrons.
- $Q_{\mathrm{total}} > 80$ pC to eliminate muons.
- Tracking $\psi^2 < 1.0$ for both x and y directions.
- The momentum should lie within $3\sigma(\pm 1$ GeV) from the nominal beam momentum.

The measured raw charge of each PMT was normalized to the DU current as described in section 5, with the measured Q_{HAC2} divided by 1.01. The muon studies showed that the gains between the two HAC sections are slightly different.

In addition, since four modules were read out and the beam was incident on the center of the second from the top, the bottom module was used as a veto to exclude events. The total charged deposited in the bottom module was required to be less than 2.5 pC. Because the BAC resolution is significantly worse than the BCAL, and there was inactive material between BCAL and BAC, only the events with no leakage in the BAC were used to determine the α parameters. The energy deposited in BAC was required to be less than 0.25 GeV to be consistent with pedestal response. It was also required that $Q_{\mathrm{HAC2}}/Q_{\mathrm{total}} < 0.1$ to limit the bias from the missing energy deposited in the inactive region. This last cut removed very few events and had a negligible effect on the results.

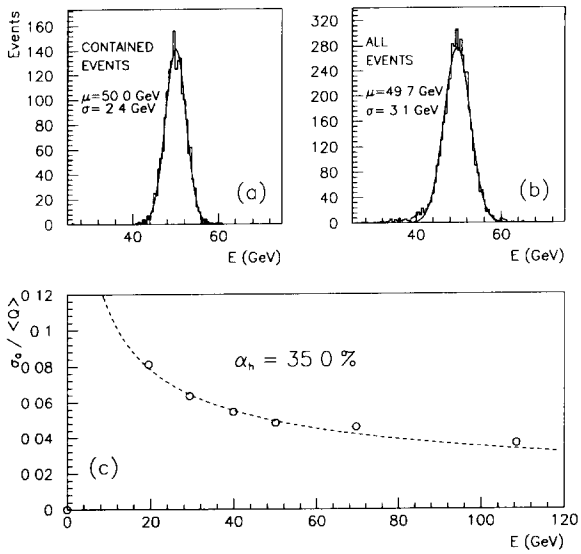

Fig. 20. (a) Reconstructed energy distributions for 50 GeV pions Only events with fully contained showers were included. The resolution calculated from this plot is about $35\%/\sqrt{E}$. (b) The deposited energy in the BAC was added to the energy calculation and no containment cut was applied to the data. The measured resolution is about $43.6\%/\sqrt{E}$, mainly due to the $100\%/\sqrt{E}$ BAC resolution. (c) The relative error σ/E versus beam energy E for fully contained showers. The dashed line is a fit of the form $\alpha_h/\sqrt{E}$.

5.3.2.2. Resolution. Using the α parameters calculated from the energy scan, all data were included in a further analysis to measure the energy resolutions. The distribution of the reconstructed charge for 50 GeV pions is plotted in fig. 20. In fig. 20a only those events with fully contained showers were included, demonstrating a resolution of $35\%/\sqrt{E}$.

Using the energy scan data, the relative error σ_q/μ_Q was measured for the various energies and plotted versus beam momentum in fig. 20c. The plot was fitted with an $\alpha/\sqrt{E}$ form which yielded a resolution of $35\%/\sqrt{E}$. The energy resolution from the fine scan data with the substitute coil in place was $38\%/\sqrt{E}$. The energy resolutions calculated from coarse scans without coil were $35\%/\sqrt{E}$ in the central towers and $38\%/\sqrt{E}$ near the edge towers. The proximity of these towers to the edge of the module makes it probable that the worse resolution results from energy leakage through the side of the module. This is substantiated by the fact that their response was about 1.5% lower than the central tower responses. The hadron analysis results are summarized in table 6.

The BCAL mean response as a function of x and y from fine scan data was shown to vary at the 1% level. The measured linearity is within 1%.

Table 6
Results from the hadron analysis

Data set	Coil	α_h [pC/GeV]	α
19.61 GeV	OUT	$10\,31 \pm 0.07$	0.916 ± 0.009
29.00 GeV	OUT	$10\,45 \pm 0.09$	0.917 ± 0.012
39.51 GeV	OUT	10.40 ± 0.10	0.918 ± 0.013
49.79 GeV	OUT	10.56 ± 0.11	0.948 ± 0.014
70.06 GeV	OUT	10.37 ± 0.16	$0\,937 \pm 0.022$
108.88 GeV	OUT	10.52 ± 0.22	0.956 ± 0.028
Energy scan	OUT	10.43 ± 0.04	0.932 ± 0.006
Fine scan	IN	10.38 ± 0.09	0.952 ± 0.013
Coarse scan	OUT	10.51 ± 0.04	0.962 ± 0.006

With the antiproton trigger, the reconstructed energy at 50 GeV is 1.8% higher than that of the pion data. This is likely due to the excess energy that comes from the proton antiproton annihilation. Since the antiproton contamination in hadron triggers was less than 5%, this has negligible effect on the determination of the α_h.

5.3.2.3. Systematic checks. Leakage from the back of the calorimeter will affect the energy resolution both because a significant part of the energy is lost in the backbeam dead material and therefore is not sampled, and also because the backing calorimeter has a much worse hadronic resolution. If the resolution is measured by including all events without any leakage cuts, the result is worse than $40\%/\sqrt{E}$ in the beam momentum range between 20 and 110 GeV, while the nonlinearity remains better than 1%. As an example, fig. 20b shows the reconstructed energy distribution for 50 GeV πs without containment cuts, yielding a resolution of about $43.6\%/\sqrt{E}$. Fig. 21 plots the hadronic resolution (%) as a function of beam momentum (GeV) for two sets of data; the fully contained shower events (open circles), and the events where no containment cuts

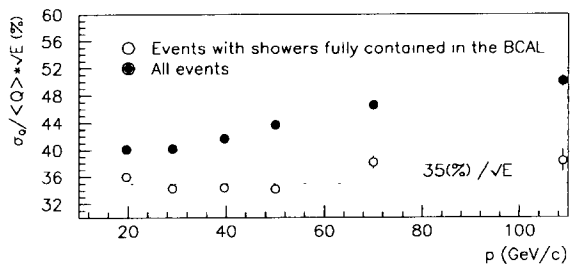

Fig. 21. the hadronic resolution (%) as a function of beam momentum (GeV) for two sets of data; the fully contained shower events (open circles) and the events where no containment cuts have been applied (full circles). The contained events show that the resolution is approximately independent of the beam momentum, while the non-contained events exhibit a resolution that deteriorates with increasing energy.

have been applied (full circles). The contained events show that the resolution is approximately independent of the beam momentum, while the non-contained events exhibit a resolution that deteriorates with increasing energy, consistent with the assumption that the resolution is adversely affected by leakage into the BAC.

In order to determine the bias introduced by the $E_{\mathrm{HAC2}}/E_{\mathrm{total}}$ cut, the cut was varied between having no cut in the HAC2 deposited energy and the other extreme where the shower is largely electromagnetic, $E_{\mathrm{EMC}}/E_{\mathrm{total}} > 0.7$. Between these two extreme cases, $10.42 < \alpha_h < 10.47$ (pC/GeV), and $0.926 < \alpha < 0.939$.

5.3.2.4. e/π. The e/π ratio was also calculated using the response to electrons and to hadrons as they are derived from the energy scans. The nominal beam energies at which data were taken were different for electrons and hadrons, requiring corrections in the analysis. Also, electron data were confined to the central area of the EMC towers. In the hadron case no such cut was made. Two numbers are quoted for e/π, one with electron response measured at the center of the towers, $e_{max}/h = 1.03 \pm 0.03$, and one that uses an average response for the electrons, $e_{ave}/h = 1.00 \pm 0.03$. The error on these values comes primarily from the variation of the intercalibration constant, α, as they were calculated from different data samples.

For a compensating calorimeter, the response should be the same for showers with different electromagnetic shower content, provided the shower is always fully contained. In fig. 22, the reconstructed energy in GeV is plotted against the ratio of deposited energy into the EMC for 30 and 50 GeV pions. The horizontal lines are plotted at $\pm 2\%$ away from the mean energy and give an indication of the deviation of e/π from unity.

5.4. Position resolution

The spread of the electron shower can be exploited to give a measure of the electron's point of entry into the calorimeter. The drift chambers provided an independent measurement of the entry point, with resolutions in both x and y of about 1 mm. This position was used to calibrate the position found by the calorimeter.

In the x direction, energy sharing between towers is used to find the position, while in y the position is estimated from energy sharing between phototubes on opposite sides of the same tower. To find the position from the calorimeter data, an asymmetry was defined for both x and y by $(Q_1 - Q_2)/(Q_1 + Q_2)$. In the x direction, Q_1 and Q_2 were the energies in the towers to the immediate left and right of the struck tower. In the y direction, Q_1 and Q_2 were the lower and upper phototubes within the struck tower, summed with its immediate neighbors. (In the case that the particle struck near the interface between two modules, the upper tube in the lower module and lower tube in the upper module were defined as Q_1 and Q_2.)

Typical distributions of the asymmetry versus the value of x measured by the tracking is shown in fig. 23. Superimposed are the fitted curves used to parametrize the dependence. A total of six parameters were required to describe the dependence on y, while for x a four-parameter fit was sufficient. The resulting fit parameters were used to reconstruct the position of individual electrons from a different electron data sample.

In x, six different electron energies, ranging from 8 to 90 GeV, were available for study. The position resolution was defined as the σ of a Gaussian fit to the distribution of differences of position found by the

Table 7
e/π values calculated from energy scans. For explanation of the various symbols refer to text

e_{max}/π	1.03 ± 0.03
e_{ave}/π	1.00 ± 0.03

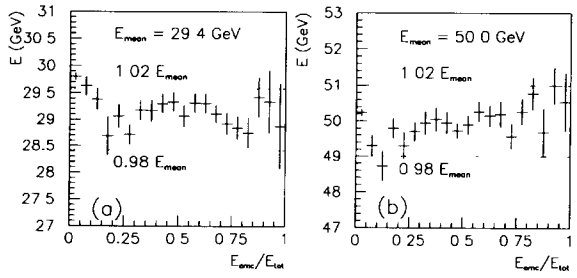

Fig. 22. Reconstructed energy (GeV) for fully contained events versus the ratio of deposited energy into the EMC. (a) 30 GeV and (b) 50 GeV. The horizontal lines are plotted at $\pm 2\%$ from-the mean energy and give an indication of the systematic errors in the determination of α.

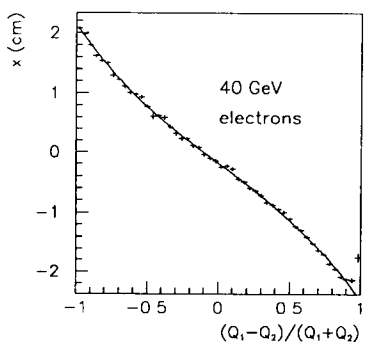

Fig. 23. A typical distribution of the asymmetry versus the value of x measured by the tracking. Superimposed is a four-parameter fit function.

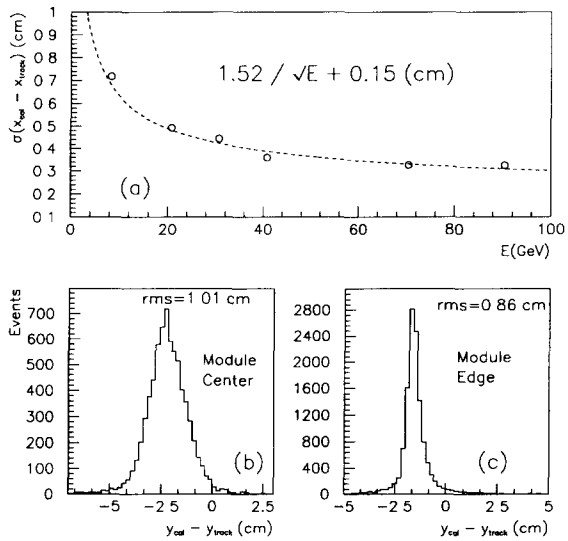

Fig. 24 (a) The position resolution in x, plotted versus energy. The dashed curve is given by $1.52/\sqrt{E}+0.15$ in cm. The constant term comes in part from the drift chamber resolution. (b) Distribution of the error in position determination, position measured by the calorimeter minus position from tracking. (c) Same plot for y positions close to the edge of the tower.

calorimeter and by the drift chambers. The distribution of the position resolution versus energy, shown in fig. 24a, was fitted with the form α (cm)$/\sqrt{E(\mathrm{GeV})}+\beta$ (cm) with resulting values $\alpha = 1.52$ cm and $\beta = 0.15$ cm. The constant term comes in part from the drift chamber resolution.

In y, only one energy (40 GeV) was available for the study. The resolution for the y coordinate, defined as above, is 0.45° when the energy is localized within one module, and 0.37° when energy is shared between two modules. The better resolution in the second case is due to the greater proximity of the phototubes in adjacent modules. Figs. 24b and 24c show the resolutions in y at the edge and center of a calorimeter tower. Since the position resolution in y should also improve as $1/\sqrt{E}$, the measured position resolution in the center of the tower corresponds to 5.2 cm$/\sqrt{E}$, and that at the tower edge corresponds to 4.0 cm$/\sqrt{E}$.

5.5. Measurements of attenuation length

The variation in response as a function of y, which measures the distance away from the wavelength shifter along the scintillator tiles, can be used to determine the attenuation length (L) of the scintillator. The responses of the left and right PMTs can be used to separately determine L, by fitting the y-dependence for the left PMT with the function $Q_l(y) = A \exp(y/L)$ and the right side with $Q_r(y) = A \exp[(y_0 - y)/L]$, where y_0 is the width of module at its front end. Afternately, one can fit the ratio of the left and right responses with the form

$$\frac{Q_r}{Q_l} = A \exp\left(-\frac{2y}{L}\right). \tag{19}$$

This method was found to decrease the effect of statistical fluctuations. The consistency of the results of the two methods, which agreed at the level of about ±10%, are indicative of the systematic errors in the measurement of L.

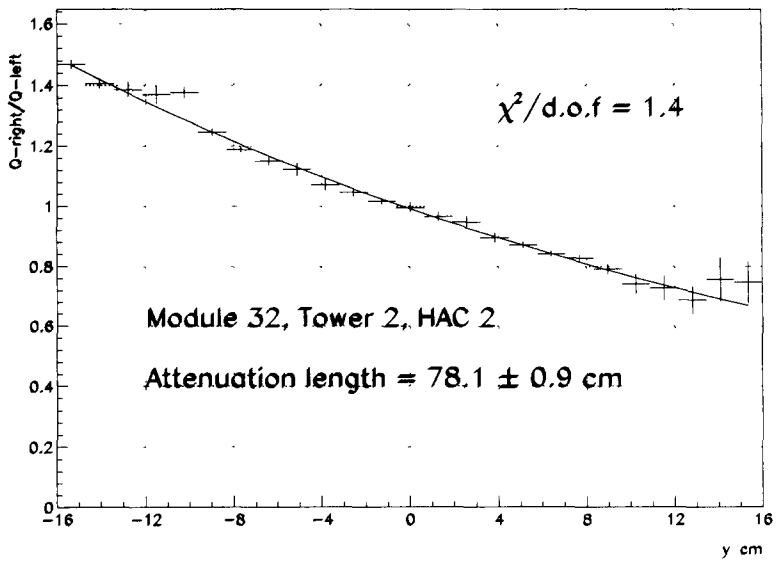

Fig. 25. Ratio of the right to left responses to muons as a function of y for HAC2 tower 2 in module 32.

Table 8
Summary of measurements of attenuation length

Module number	Tower type	Tower number	Data set	Attenuation length [cm]
8	EMC	19	Muon	53.7 ±2.0
26	EMC	33	Electron	54.53±0.4
26	EMC	43	Electron	54.67±0.4
26	EMC	44	Electron	54.55±0.4
1	HAC1	2	Muon	73.2 ±2.0
3	HAC1	8	Muon	75.6 ±0.9
32	HAC1	1	Muon	77.6 ±1.1
32	HAC1	2	Muon	78.4 ±1.4
1	HAC2	2	Muon	70.4 ±1.2
32	HAC2	1	Muon	78.7 ±0.7
32	HAC2	2	Muon	78.1 ±0.9

For the EMC towers, L can be measured using either muon or electron beams, while only muon beams are available for the determination of L for the HAC towers. In the muon data analysis, the truncated mean algorithm was used to calculate the muon response.

5.5.1. HAC tower results

For HAC2, an additional factor needs to be taken into account before the attenuation lengths can be calculated. The PMTs are coupled to the wavelength shifter at the back of HAC2 by means of plastic "cookies" which emit Cherenkov radiation when charged particles pass through them. Therefore for those positions in the fine scan where the beam is centered on one of the PMTs, the response is enhanced due to the additional light. Given the tapered geometry of the module, this effect is only seen for HAC2. The effect is removed by excluding muons from the fit which hit in the region of the PMT.

Fig. 25 shows the ratio of the right to left responses (Q_r/Q_l) as a function of y for a typical tower, a curve which is much more uniform than those of the left or right individually. The measured attenuation lengths are very consistent between towers as well as between the two sections of the HAC, and have an average value of approximately 75 cm as shown in table 8. Module 1 is seen to have lower attenuation length compared to module 32. This reflects startup construction differences associated with the first few modules. The same effect was also seen in enhanced light yield of the later modules as is discussed in the next section.

5.5.2. EMC tower results

Measurements of attenuation for EMC cells were made with electrons and with muons. The two techniques yielded consistent values of attenuation length of the scintillator in the EMC towers.

EMC tower 19 of module 8 was used to determine the attenuation length of the scintillator with muons. Fitting the left and right responses yields consistent values for the attenuation length of 53.7 ± 1.9 cm, and 53.6 ± 2.0 cm. Using electrons, the ratio of left to right EMC energy was calculated and fitted. The resultant value of the attenuation length is consistent with the muon results, as summarized in table 8.

5.6. Further studies

As described below, analyses of the muon data included a determination of the light yield of the BCAL modules, and a comparison of the muon response, and its energy dependence, with results of a Monte Carlo simulation.

5.6.1. Light yield

The number of photoelectrons for the HAC was determined using the muon coarse scan data. In addition to the cuts used to ensure good muons, the muons were required to pass through the center of the module in y within ±1 cm. Thus it was not necessary to correct for the variation of optical attenuation with position.

The number of photoelectrons per GeV of deposited energy per calorimeter cell (right and left PMTs), N_{pe}, is given by an equation analogous to eq. (13):

$$N_{pe} = \frac{1}{\alpha_e} C \frac{1}{\langle Q_c \rangle} \left(\frac{\langle Q_c \rangle}{\sigma_c} \right)^2, \tag{20}$$

where $\alpha_e = 10.73$ pC/GeV is the conversion factor measured from the electron data, $\langle Q_c \rangle$ is the average cell charge over a module section, and σ_c is the width of the charge distribution arising from photostatistics. Operationally, σ_c is calculated as the Gaussian width of the charge difference distribution between the photomultipliers on opposite sides of the tower. The width of the charge sum distribution is not used because it has a substantial contribution from the Landau shape in addition to that arising from photostatistics. The parameter $C = 1.11$ is a correction factor for the effects of photostatistics at subsequent dynodes of the PMT. It will be noticed that $N_{pe} = 2n_{pe}$, where n_{pe} was defined in section 4.5.

The charge spectrum has an approximately Landau distribution with a large high energy tail. To eliminate the effect of statistical fluctuations and possible backgrounds in the high energy tail as well as the non-Gaussian tails of the charge difference distribution, the charge spectrum was truncated at a maximum charge of 30 pC. Note that the number of photoelectrons produced per GeV is independent of which region of the charge spectrum is used, and therefore N_{pe} can be determined from any part of the spectrum. The quantity N_{pe} was calculated for each tower in a module, for

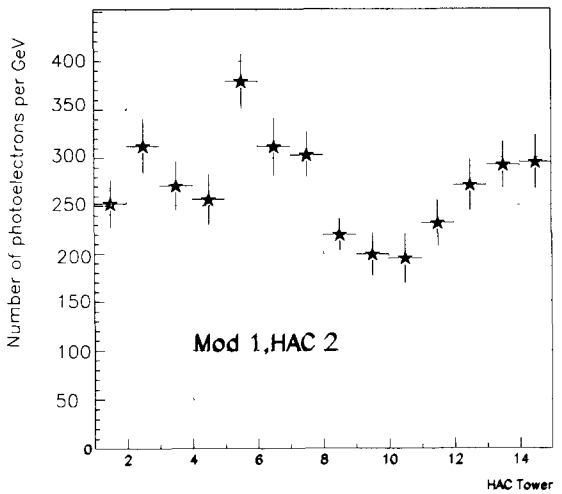

Fig. 26. Photoelectron yield versus HAC2 tower in module 1 from the 1990 run

HAC1 and HAC2 separately, and then averaged over the towers in the module. The errors in the quoted numbers reflect the tower-to-tower variation of the response as well as the statistical uncertainty.

Fig. 26 shows the photoelectron yield for the towers in a typical module for the 1990 run. Table 9 shows the photoelectron yield for the modules tested in 1990/91. Also shown for comparison are results from the analysis of data obtained by pulsing the module with a laser flasher system [17].

The mean charge, $\langle Q_c \rangle$, is higher for the 1991 data because higher energy muons (100 GeV) were used than in 1990 (50 GeV). These measurements are consistent with measurements made during the cosmic ray checkout [4] as well as the measurements made using the laser [17]. The construction technique for the first few modules (especially 1 and 3) was slightly different from that used for the remainder. This may be the reason why the number of photoelectrons is lower for these modules.

Table 9
Number of photoelectrons per cell per GeV of deposited energy for the HAC1 and HAC2 towers The laser results come from measurements taken in Fermilab

Module number	p_{Beam} [GeV/c]	Tower type	$\langle Q \rangle$ [pC]	N_{pe} [GeV^{-1}]	$N_{\text{pe}}^{\text{Laser}}$ [GeV^{-1}]
1	50	HAC1	8.99±0.16	182±32	172±43
		HAC2	9.19±0.11	161±32	182±43
3	50	HAC1	9.17±0.11	140±21	150±32
		HAC2	9 20±0.17	161±32	172±43
8	50	HAC1	8.99±0.21	161±32	NA [a]
		HAC2	9.00±0.20	203±32	NA [a]
12	100	HAC1	9.87±0.09	247±43	247±21
		HAC2	10.00±0.10	257±43	247±21
26	100	HAC1	9.99±0.09	279±32	300±21
		HAC2	10.12±0 10	311±43	343±21
32	100	HAC1	10.17±0.08	311±32	311±32
		HAC2	10.15±0.09	311±43	343±21

[a] NA = not available.

Table 10
N_{pe} as a function of incident muon energy for HAC1 and HAC2 towers

Beam momentum [GeV/c]	HAC1		HAC	
	$\langle Q \rangle_T$ [pC]	N_{pe} [GeV^{-1}]	$\langle Q \rangle_T$ [pC]	N_{pe} [GeV^{-1}]
30	8.82±0.03	251.1±4.3	8.83±0.03	284.3±4.3
50	9.29±0 03	260.0±4.3	9.37±0.03	294.0±5.4
70	9.71±0.04	260.0±4.3	9.74±0.04	296.1±5.4
100	10.24±0.02	258.6±1.1	10.28±0.02	292.9±2.1

5.6.2. Muon energy scan results

To verify that N_{pe} is independent of incident energy, and to check the procedure used to calculate N_{pe}, module 26 was placed in the θ–ϕ stand and data were collected with muon energies of 30, 50, 70 and 100 GeV. The beam was centered in the middle of HAC tower 9. The truncated mean charge, Q, was calculated after DU correction for the total charge distribution from the tower. This value was then compared with the Monte Carlo simulation results as described later. The same data were also analyzed to obtain the number of photoelectrons per GeV.

Since the energy scan data were collected with the module in the θ–ϕ stand, there was some degree of contamination of the muon beam by pions. Thus, there were a number of events with large energy deposits from hadronic interactions in the HAC. The procedure using the truncated mean rejected these hadronic events. The contamination of the truncated sample was negligible. The results are presented in table 10. As expected, N_{pe} is energy independent within errors.

The errors on N_{pe} for the "energy scan" runs are considerably smaller that those for the "coarse scan" runs because the average N_{pe} for each module reflects the statistical-error as well as the systematic tower-to-tower variation in the module, while the "energy scan" runs are for a single tower. In addition, the statistics for the "energy scan" runs were larger than those for the "coarse scan" runs by almost an order of magnitude.

For comparison, the corresponding values of N_{pe} from the coarse scan analysis for module 26 tower 9 are 278 ± 15 for HAC1 and 296 ± 15 for HAC2. These values are in agreement with the energy scan measurements.

The detector simulation package GEANT [18] was used to simulate the geometry of the module and study

its response to incident muons. The geometry coded was that of a section three times the size of a tower in both transverse dimensions in order to study the sharing of energy between towers. The energy deposited in the central tower was then used in the study. The momentum spectrum of the incident muon was modeled on the one measured for data at 50 GeV, which included asymmetric tails in the momentum distribution. The composition of the tower, with layers of depleted uranium/stainless steel cladding and scintillator was incorporated into the setup. The simulation was configured to include explicit δ-ray production and tracking through the detector. The visible energy deposited in the calorimeter for all three sections, EMC, HAC1 and HAC2, was recorded for the passage of a muon with a given momentum through the tower, allowing for standard energy loss and multiple scattering, muon–nucleus interactions, etc.

The visible energy spectrum from the Monte Carlo had to be smeared for the spread due to finite photoelectron statistics using the average number of photoelectrons per MeV of deposited energy. The smearing was done using a Gaussian instead of a Poisson distribution, since typically more than 100 photoelectrons are produced in the HAC.

To compare data and Monte Carlo, the most probable values of the two were made to coincide for the 50 GeV point. Next, the number of events in the region 0 to 100 GeV was normalized to be equal for data and Monte Carlo for all energies. The Monte Carlo data were then smeared with the measured number of photoelectrons for that tower.

The mean truncated charge, Q, for the data and Monte Carlo, as a function of the energy are shown in fig. 27a for HAC1 and 27b for HAC2. The Monte Carlo spectrum has been smeared assuming 257 photoelectrons/GeV for HAC1 and 300 photoelectrons/GeV for HAC2.

The data for 30 and 70 GeV muons is shown in fig. 28 for HAC1, with Monte Carlo expectations shown by the dashed curve. For high energies (above 70 GeV) there is some discrepancy between the data and Monte Carlo. Some of the difference was found to be due to the cutoffs in electromagnetic energies used in the GEANT simulation.

5.7. Beam induced DU activation

In analyzing the data from the August 1990 data taking period, it was found that the uranium activation by the beam continued to have effect long after the spill was completed. As can be seen from fig. 29, there is a clear remnant effect at the level of several percent even 8 s after beam turnoff, when the DU current is read. This phenomenon was caused by typical beam intensities of $1\text{–}5 \times 10^5$ particles per spill. It affected

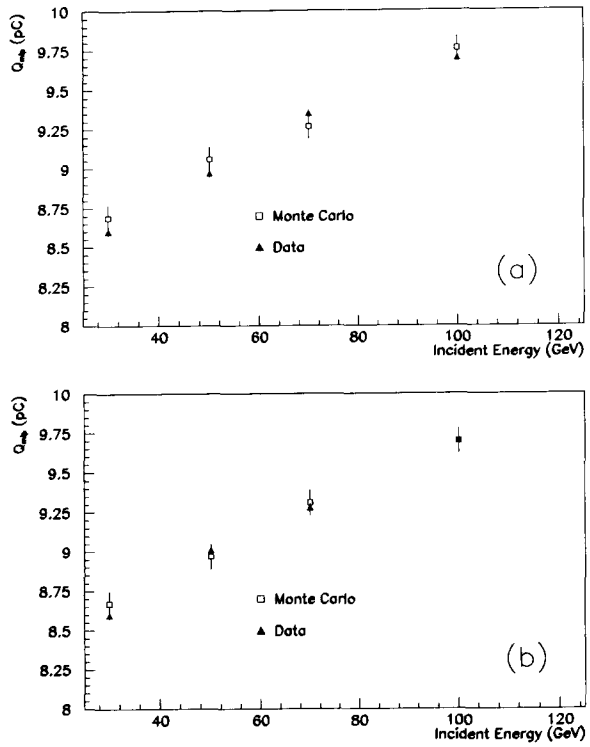

Fig. 27. The mean truncated charge, for the data and Monte Carlo as a function of the energy for (a) HAC1 and (b) HAC2.

the θ–ϕ studies because the modules were hit directly by the beam. Hadron trigger runs were not affected, however, because data were taken with the upstream beam collimators almost closed. In the 1991 data tak-

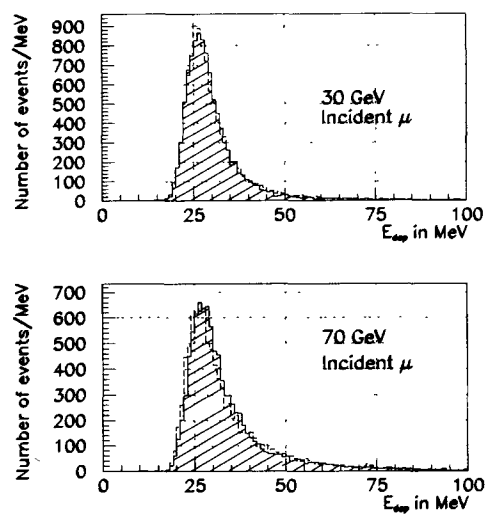

Fig. 28. Distribution of collected charge for 30 and 70 GeV muons in HAC1. The solid lines are data while the dashed lines are Monte Carlo results.

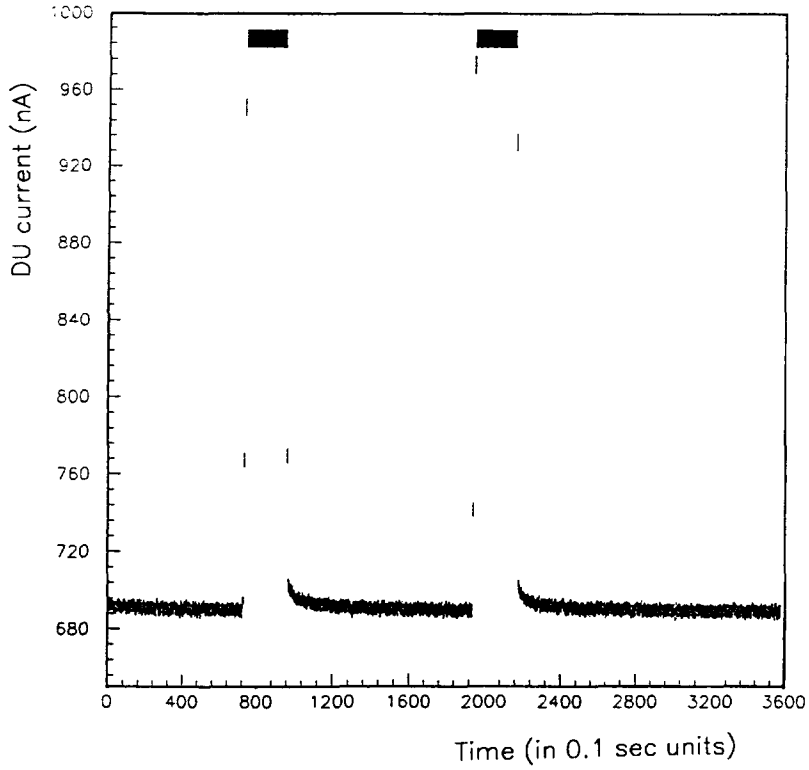

Fig. 29. Measurements of the DU current taken at a rate of 10 Hz. It happened that there was beam only during two spills due to machine aborts. During the spill the DU scale saturated.

ing period the intensities were purposefully much lower, and DU activation was not observed.

After attempting to extract DU currents in different ways, it was decided to utilize the DU information during the period in which the data were taken. It was assumed that the measured DU current of PMT j after spill i, I_{ij}^{m}, relates to the constant DU current in the absence of beam, I_j, through

$$I_{ij}^{\mathrm{m}} = I_j f_{ij}, \tag{21}$$

where f_{ij} is the correction term for the presence of the beam.

The correction term was assumed to depend on a time constant characteristic of the DU activation τ, the spatial spread of the beam σ, the magnitude of the effect C, and the 106 parameters describing the DU current for the 106 EMC PMTs I_j. The following form was chosen:

$$f_{ij} = 1.0 + 100C \sum_{k=1}^{i-n} A_k \, \mathrm{e}^{-\frac{(x_k - x_j)^2}{2\sigma^2}} \, \mathrm{e}^{-\frac{(t_i - t_k)}{\tau}}, \tag{22}$$

where the sum extends for n spills up to and including the present (ith) one. The parameters τ, σ, C, I_j are to be calculated and the rest of the variables are available from the data. The variable A_k is the beam intensity of the kth spill in units of 2×10^5, x_k the centroid of the beam in that spill in tower number units, t_k the time of the kth spill, x_j the tower number for which the DU current is measured and t_i the time of the ith (present) spill.

Using the fact that the dependence on each of the I_j is linear and independent of the others, the best measure of I_j, with τ, σ and C fixed, is:

$$I_j = \frac{\sum_k f_{jk} I_{jk}^{\mathrm{m}}}{\sum_k f_{jk}^2}. \tag{23}$$

Three runs were used to calculate the τ, σ and C parameters; an electron coarse scan, a muon coarse scan, and a hadron scan of a few towers. The parameters obtained from each run together with the rms

Table 11
Results of the calculation on the effect of the DU activation

Run type	C 2×10^5	σ towers	τ spills	σ_1 [nA]	NDF
Electron coarse scan	1.116	1.73	0.66	0.386	10611
Muon coarse scan	0.978	1.54	0.60	0.333	5791
Hadron scan	0.875	1.95	0.85	0.269	12505
Average	0 992	1.74	0.704	–	–

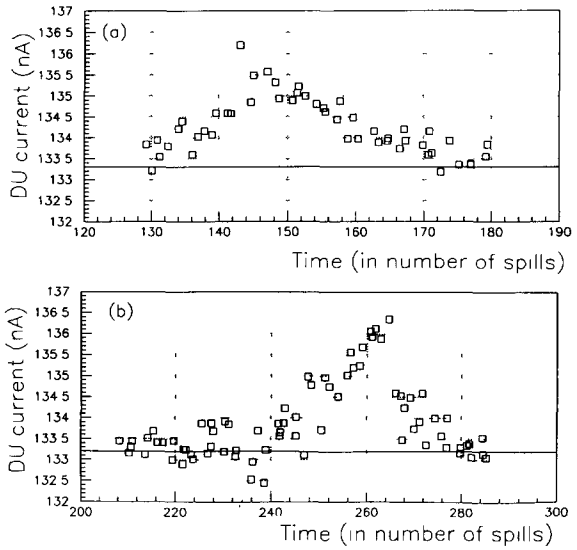

Fig. 30. DU current as a function of spill number for two typical towers. The peak due to the DU activation is clearly visible. The horizontal line is the DU value calculated by the minimization procedure. (a) Right side, tower 27, module 2. (b) Left side, tower 47, module 2. See text for more details.

value for the DU residual, σ_I, obtained by setting the χ^2 equal to the number of degrees of freedom NDF, are tabulated in table 11.

Use of the average parameters, in the last row of table 11, resulted in changes in the values of I_j of less that 0.1 nA in all cases. Applying these calculated parameters to a different run, with a different module, demonstrated a dispersion of the residuals equal to 0.5 nA. This indicates that the precision of this technique should be better than 1%. Fig. 30 shows the DU current as a function of spill number for two typical towers. The x-axis can be considered to be the time in minutes (one spill per minute), with left being earlier times. The θ–ϕ stand rotates to expose a different tower to the beam. Therefore, the plotted tower in the beginning and in the end does not see any beam. The peak due to the DU activation when the beam hits the tower is clearly visible. The horizontal line is the DU value calculated by the minimization procedure.

Most of the results in this report were derived from 1991 data when there was no DU activation. Some data were also used from the high beam intensity period. In this case the DU correction was based on the above algorithm.

6. Conclusions

Several modules of the ZEUS BCAL were tested in a test beam environment and the absolute calibration was established. All subsystems in the BCAL were tested in detail. Measurements were also taken with an aluminum bar in front of the BCAL to simulate the ZEUS superconducting coil. Experience was gained with the read out electronics operation, calibration and monitoring. Electrons, pions, muons, and antiprotons of energies between 6 and 110 GeV were used in the process. The obtained results are as follows.

– Charge reconstruction accuracy of the electronics using charge injector events was within 0.2%.

– Linearity of the electronics was found to be within 0.2% in the complete charge injector range.

– Stability of the DU current was at a level of 1% over a 40 h period.

– Linearity of the HV system using the laser was found to be better than 1% over a range between 40 and 250 GeV.

– Noise level in the calorimeter per PMT was 8.6, 16.3, and 18.0 MeV for the EMC, HAC1, and HAC2 channels, respectively, and was dominated by uranium activity. The noise between the two PMTs on one tower is thus partially correlated, and the total noise is 14.4, 29.0, and 32.2 MeV for cells in the three calorimeter sections.

– Light yield using the laser was measured to be 78 ± 20 and 122 ± 27 photoelectrons per PMT per GeV for the EMC and HAC towers respectively. The calculation was repeated using muon data and the results agree within errors.

– Tower uniformity. Using muons, the average tower-to-tower uniformity was 1.1%. From the electron data, the average uniformity was 1.0%. By averaging all tower responses in a module, it was found that the responses of two modules were within 0.3–0.5%.

– Attenuation lengths using the electrons and muons were calculated for several modules. The attenuation length in the EMC is about 54.6 ± 0.23 cm and in the HAC towers 76.0 ± 1.2 cm.

– Position measurement using the calorimeter gives a resolution 1.53 cm/$\sqrt{E}$ in the x-direction. In the y-direction, it was found that the position resolution is 5.2 cm/$\sqrt{E}$ near the middle of the tower, and 4.2 cm/$\sqrt{E}$ near the edge of the modules.

– The response to muons was found to be 3.27 pC/mip for an EMC tower (2 PMTs), 9.34 pC/mip for HAC1, and 9.41 pC/mip for HAC2. The EMC data were taken with 50 GeV muons and the HAC data with 100 GeV muons.

– The response to electrons for the particular set of gains was 10.74 pC/GeV when the electrons hit the calorimeter directly, and 10.54 pC/GeV when the equivalent ZEUS coil material was placed in front of the module. These numbers were calculated using electrons that hit away from the tower edge where the dead material reduces the response of the calorimeter.

– The response to hadrons were measured to be 10.43 pC/GeV without the equivalent ZEUS coil material and 10.38 pC/GeV with coil material.

– The e/π ratio was 1.00 ± 0.03 when the average response to electrons was taken into account.

– The linearity of response to electrons was found to be within 1% for beam energies in the range between 6 and 90 GeV.

– The linearity of response to hadrons was found also to be within 1% for beam energies in the range between 20 and 110 GeV.

– The electromagnetic energy resolution was found to be $19.1\%/\sqrt{E}$ without the coil, and $20.2\%/\sqrt{E}$ with the coil in place.

– The hadronic energy resolution was measured to be $35\%/\sqrt{E}$ for fully contained events. The coil material degrades the resolution to $38\%/\sqrt{E}$.

Acknowledgements

These results would not have been possible without the very strong support of the Fermilab administration. Special thanks to J. Peoples, P. Garbincius, H. Montgomery, and T. Yamanuchi. G. Koizumi was indispensable in the effort to deliver beam to the experiment and C. Hojvat made sure that needs were met in the best possible way. We owe special gratitude to K. Gray for essential support. C. Billups saw that operations in the Lab F were efficient and safe. Also thanks go to colleagues who worked to maintain modules and on the first stages of the experiment, including G. DeClute, J. Kehres, and P. Nylander from Univ. of Wisconsin; W.G. Liou and W.J. Xu of Univ. of Iowa; R. Stanek from ANL; W. Sippach, H. Cunitz, J. Xu, F. Xu and D. Chen from Columbia Univ.; and R. Nolty, D. Asner, W.W. Lu, and X. Shi from California Institute of Technology.

References

[1] H. Brückmann, B. Anders and U. Behrens, Nucl. Instr. and Meth. A 263 (1988) 136.

[2] E. Bernardi et al., Nucl Instr. and Meth. A 262 (1987) 229;
G. d'Agostini et al., Nucl. Instr. and Meth. A 274 (1989) 134;
U. Behrens et al., Nucl. Instr. and Meth. A 289 (1990) 115;
A. Caldwell et al., Development of the Front End Electronics for the ZEUS High Energy Calorimeter, Proc. Workshop on Calorimetry for the Supercollider, Tuscaloosa, Alabama, March 13–17, 1989.

[3] A. Andresen et al., Nucl Instr. and Meth. A 309 (1991) 101

[4] I. Ambats et al , Nucl. Instr. and Meth. A 320 (1992) 161.

[5] M. Derrick et al., Nucl. Instr. and Meth. A 309 (1991) 77.

[6] B.G. Bylsma et al., Nucl. Instr. and Meth. A 305 (1991) 354.

[7] A. Caldwell et al., Nucl. Instr. and Meth. A 321 (1992) 356.

[8] B. Lu, L.W. Mo and T A. Nunamaker, Nucl. Instr. and Meth A 313 (1992) 135;
ZEUS-Note-88–036 and AMZEUS Note 56, 1988.

[9] W.K. Sakumoto et al., Nucl. Instr. and Meth. A 294 (1990) 179.

[10] C. Foudas, Nevis report 272 (1989); R-1421 CU378 NEVIS 272.

[11] J. Lach and S. Pruss, Fermilab Publication TM-298 2254.000, April 28, 1971.

[12] S. Park, ZEUS note 91-045 (1991).

[13] T. Woeniger, DESY 90-024, March 1990;
H. Boterenbrood et al., Nucl. Instr. and Meth. A 332 (1993) 263.

[14] A. Bernstein, A Caldwell, E. Ros and T. Tsurugai, ZEUS note 91-114, December 9, 1991.

[15] R. Loveless, WISC-EX-93-329.

[16] L. Chen et al., ZEUS note 92-023, April 2, 1992.

[17] J. Whitmore et al., AMZEUS note AMZEUS-103, PSU LEPS Memo No. 306, March 23, 1990.

[18] R. Brun et al., CERN DD/EE/84-1 (1986).